CM 2002-007

# Numerical investigation of the meso-mechanical behavior of concrete under impact tensile loading

October 2002

W.Y. Liu and L.J. Sluys

# REPORT DOCUMENTATION PAGE

Form Approved OMB No. 0704-0188

| 1. REPORT DATE *(DD-MM-YYYY)* | 2. REPORT TYPE | 3. DATES COVERED *(From – To)* |
|---|---|---|
| 01-10-2002 | Final Report | 20 November 2000 - 20-May-01 |

**4. TITLE AND SUBTITLE**

Micro-mechanical study to the behavior of heterogeneous materials under impact loading

**5a. CONTRACT NUMBER**
F61775-01-WE002

**5b. GRANT NUMBER**

**5c. PROGRAM ELEMENT NUMBER**

**6. AUTHOR(S)**

Dr Lambertus Sluys

**5d. PROJECT NUMBER**

**5d. TASK NUMBER**

**5e. WORK UNIT NUMBER**

**7. PERFORMING ORGANIZATION NAME(S) AND ADDRESS(ES)**
Delft University of Technology
Stevinweg 1
Delft 2628 CN
The Netherlands

**8. PERFORMING ORGANIZATION REPORT NUMBER**
N/A

**9. SPONSORING/MONITORING AGENCY NAME(S) AND ADDRESS(ES)**

EOARD
PSC 802 BOX 14
FPO 09499-0014

**10. SPONSOR/MONITOR'S ACRONYM(S)**

**11. SPONSOR/MONITOR'S REPORT NUMBER(S)**
SPC 01-4002

**12. DISTRIBUTION/AVAILABILITY STATEMENT**

Approved for public release; distribution is unlimited.

**13. SUPPLEMENTARY NOTES**

**14. ABSTRACT**

This report results from a contract tasking Delft University of Technology as follows: The contractor will investigate the mechanical behavior of brittle heterogeneous materials such as concrete extreme dynamic loading conditions. The contractor will develop a mathematical model of brittle heterogeneous materials under extreme dynamic loading conditions to accurately predict civil engineering structural responses not well predicted by existing quasi-static models.

**15. SUBJECT TERMS**
EOARD, Materials, Deformation analysis, Failure Mechanisms, High Strain Rate

| 16. SECURITY CLASSIFICATION OF: | | | 17. LIMITATION OF ABSTRACT | 18, NUMBER OF PAGES | 19a. NAME OF RESPONSIBLE PERSON |
|---|---|---|---|---|---|
| a. REPORT | b. ABSTRACT | c. THIS PAGE | UL | | Charles H. Ward, Lt Col, USAF |
| UNCLAS | UNCLAS | UNCLAS | | 47 | 19b. TELEPHONE NUMBER *(Include area code)* +44 (0)20 7514 3154 |

Standard Form 298 (Rev. 8/98)
Prescribed by ANSI Std. Z39-18

# Numerical investigation of the meso-mechanical behavior of concrete under impact tensile loading

October 2002 <u>W.Y. Liu and L.J. Sluys</u>

# Preface

This research was conducted at the Department of Civil Engineering and Geosciences of Delft University of Technology. The project was sponsored by the European Office of Aerospace Research and Development (EOARD), Air Force Office of Scientific Research (AFOSR), Air Force Research Laboratory (AFRL), under Contract No.F61775-01-WE002.

The Contractor, Delft University of Technology, hereby declares that, to the best of its knowledge and belief, the technical data delivered herewith under Contract No.F61775-01-WE002 is complete, accurate, and complies with all requirements of the contract.

DATE: *30 - 9 - 2002*

Name and Title of Authorized Official: *prof.ir. C.P.J.W. van Kruijsdijk*

I certify that there were no subject inventions to declare as defined in FAR 52.227-13, during the performance of this contract.

DATE: *30 - 9 - 2002*

Name and Title of Authorized Official: *prof. ir. C.P.J.W. van Kruijsdijk, dean of the faculty of Civil Engineering and Geosciences*

# Contents

# Chapter 1

# Introduction

## 1.1 Purpose of this report

This report is focused on the numerical simulation of the micro-mechanical response of concrete under dynamic tensile loading. The microstructure plays an important role in the behavior of heteogeneous materials under impact loading. For instance, concrete has a higher resistance under impact loading than under static loading. This is partly due to the microstructure. The micro-mechanical background of this observation is the main topic of this report.

## 1.2 Relevant concepts

### 1.2.1 Representative volume element

In this investigation, a microstructure or *Representative Volume Element* (RVE) is used. An RVE for a material point of a continuum is a material volume which is sufficiently representative of the infinitesimal material neighbourhood of that material point (cf. [13]). It is regarded as a heterogeneous material with spatially varying, but known, constitutive properties. It is of importance that statistical properties of the state variables are considered invariant of the position in the material. This is called statistical homogeneity.

Since concrete is a highly heterogeneous material, the size and shape of the RVE should be chosen properly with respect to the dimensions of concrete structures. For example, a minimum aspect ratio, which is the ratio between the microstructure dimension and the maximum grain size, should be taken of 3 to 5 (cf. [14]). Another essential step in numerical homogenization is the appropriate choice of the microscopic boundary condition. Since the homogenization procedure is not followed, this issue is not addressed in this investigation.

### 1.2.2 Softening and localization

The main cause of the nonlinearity of concrete is cracking, which is primarily due to the limited capacity of concrete to sustain tensile stresses ( or perhaps better, tensile strains). Three main approaches can be distinguished for the modelling of cracking in concrete, namely discrete crack models, for example the cohesive surface methodology adopted by Tijssens (cf. [12]) for simulation of the fracture process of concrete at macro- and meso-level, the smeared crack models and lattice models. Within the smeared crack concept, a cracked solid is imagined to be a continuum where the notions of stress and strain remain valid. Hence, continuum constitutive models can be used (cf. [3]).

Concrete can be classified as a *softening material* which shows a reduction of the load carrying capacity accompanied by localized deformations after reaching the limit load. Experimentally obtained load-displacement characteristic exhibits a descending branch which is commonly known as *structural softening* behavior. Structural softening as global behavior is due to micro-cracking in concrete. At a certain stage of growth and coalescence of microcracks, deformations grow in a small portions of the material and the

rest of the structure tends to unload. This phenomenon is known as *strain localization* and eventually leads to the formation of macroscopic cracks.

For a continuum description of structural softening behavior or strain localization phenomenon, a material law with a negative slope after the limit load is used. This is called a *strain softening material law*.

### 1.2.3   Regularization methods

Unfortunately the field equations that describe the motion of the body lose hyperbolicity and become elliptic as soon as strain softening occurs, when a standard rate independent continuum model is combined with a strain softening law. The domain is split up into an elliptic part, in which waves have imaginary wave speeds and are not able to propagate (*standing waves*), and into a hyperbolic part with propagating waves. The initial value problem becomes ill-posed and can no longer be a proper description of the underlying physical proplem. Localization zones stay confined to a line with zero thickness (or a discrete plane in a three dimensional continuum). The energy consumed in the failure zones is zero. These two results are in contradiction with experimental results. In numerical simulation, the finite element tries to capture the localization zone with zero thickness which results in a mesh sensitivity. The reason for this fact is that the adopted softening laws are deduced phenomenologically and contain no actual information on the microscopic behavior of the material, which plays an important role during failure process (cf. [11]).

In order to properly model the softening solid within continuum framework, a few approaches have been proposed to regularize the governing equations, such as fracture energy based models, rate dependent models, nonlocal models, gradient models, micro-polar models (e.g. Cosserat model), and embedded discontinuity models. The common feasure of these models is the inclusion, implicitly or explicitly, of a length scale into the field equations or the description of the material. With these approaches, well-posedness of the initial value problem can be preserved, the governing equations do not necessarily lose hyperbolicity, and a solution with real wave speeds can be obtained at the onset of strain softening. The numerical results converge to a finite size of the localization zone and nonzero energy consumption in the failure process zones upon mesh refinement. The mesh dependent solution can be avoided.

In this report, the implicit gradient dependent damage model and two rate dependent viscoplastic models will be adopted as the constitutive descripion of the RVE. A length scale is incorporated in these models which preserve mesh independence.

## 1.3   Arrangement of the contents

Chapter 2 starts with basic equilibrium, constitutive and kinematic equations for the motion of an inelastic body. The finite element discretization of the virtual work equation and implicit time integration scheme will be derived.

Chapter 3 introduces two kinds of continuum models used in this report, the continuum plasticity model and the continuum isotropic damage model. The standard elastoplastic model, Perzyna viscoplastic model, Duvaut-Lions viscoplastic model, the implicit constant gradient enhanced damage model and the strain-based transient-gradient damage model are described including the algorithmic treatment.

In Chapter 4 the numerical results of a one-dimensional simulation with the models introduced in Chapter 3 are given and the regularization effects are addressed.

In Chapter 5 the results of the numerical simulation of the dynamic response of concrete at meso-level are presented. The characteristics of each model are illustrated and compared.

The report is finished with conclusions and a discussion in Chapter 6.

# Chapter 2

# Formulation of the initial value problem

The basic structure of the initial value problem (IVP) for nonlinear solids is outlined with a restriction to small deformation gradients. We use a finite element representation of the virtual work equation to derive the semi-discrete initial value problem. A full discretization is obtained if the time integration has been carried out. An incemental-iterative Newton-Raphson procedure is used to solve the resulted nonlinear equations. Throughout this report matrix-vector notation is used.

## 2.1 Preliminary equations

We consider a body B with volume $\Omega$ and surface $\partial\Omega = \partial\Omega_t \cup \partial\Omega_u$, where $\partial\Omega_t$ and $\partial\Omega_u$ are traction and kinematic boundaries, respectively, with $\partial\Omega_t \cap \partial\Omega_u = 0$. The equations of motion without damping, the kinematic equations and the corresponding initial and boundary conditions read

$$\mathbf{L}^T\sigma + \mathbf{p} = \mathbf{R}\ddot{\mathbf{u}} \qquad in \quad \Omega \qquad (2.1)$$

$$\epsilon = \mathbf{L}\mathbf{u} \qquad in \quad \Omega \qquad (2.2)$$

$$\mathbf{u}(\mathbf{x},0) = \mathbf{u}_0 \qquad \mathbf{v}(\mathbf{x},0) = \mathbf{v}_0 \qquad in \quad \Omega \qquad (2.3)$$

$$\mathbf{u}(\mathbf{x},t) = \bar{\mathbf{u}} \qquad on \quad \partial\Omega_u \qquad (2.4)$$

$$\mathbf{t} = \mathbf{N}^T\sigma \qquad on \quad \partial\Omega_t \qquad (2.5)$$

where the differential operator $\mathbf{L}$ is defined as

$$\mathbf{L}^T = \begin{pmatrix} \frac{\partial}{\partial x} & 0 & 0 & \frac{\partial}{\partial y} & 0 & \frac{\partial}{\partial z} \\ 0 & \frac{\partial}{\partial y} & 0 & \frac{\partial}{\partial x} & \frac{\partial}{\partial z} & 0 \\ 0 & 0 & \frac{\partial}{\partial z} & 0 & \frac{\partial}{\partial y} & \frac{\partial}{\partial x} \end{pmatrix} \qquad (2.6)$$

Stress and strain vectors $\sigma$ and $\epsilon$ are represented as

$$\sigma^T = [\sigma_{xx} \quad \sigma_{yy} \quad \sigma_{zz} \quad \sigma_{xy} \quad \sigma_{yz} \quad \sigma_{zx}] \qquad (2.7)$$

$$\epsilon^T = [\epsilon_{xx} \quad \epsilon_{yy} \quad \epsilon_{zz} \quad 2\epsilon_{xy} \quad 2\epsilon_{yz} \quad 2\epsilon_{zx}] \qquad (2.8)$$

$\mathbf{u}, \mathbf{v}, \mathbf{p}, \mathbf{t}$ represent the displacement, velocity, body force and surface traction with matrix $\mathbf{N}$ related to the outward normal $\mathbf{n}$ defined as

$$\mathbf{N}^T = \begin{pmatrix} n_x & 0 & 0 & n_y & 0 & n_z \\ 0 & n_y & 0 & n_x & n_z & 0 \\ 0 & 0 & n_z & 0 & n_y & n_x \end{pmatrix} \qquad (2.9)$$

The density matrix $\mathbf{R}$ is equal to $\mathrm{diag}[\rho \quad \rho \quad \rho]$ with $\rho$ the material density.

The constitutive euqations can be given in the general rate format

$$\dot{\sigma} = \mathbf{D}^c \dot{\epsilon} \tag{2.10}$$

with matrix $\mathbf{D}^c$ containing the tangent stiffness moduli. Two types of material constitutive descriptions are used in this report, the continuum damage model and the continuum plastic model. They will be detailed in Chapter 3.

## 2.2 Weak form of the initial value problem

While Eqs. 2.1 to 2.5 describe the motion of a body in a strong sense, a weak form of these equations is obtained by setting

$$\int_{\Omega} \delta \mathbf{u}^T [\mathbf{L}^T \sigma + \mathbf{p} - \mathbf{R}\ddot{\mathbf{u}}] d\Omega = 0 \tag{2.11}$$

in which $\delta$ denotes the variation of a quantity. With the aid of Green's theorem, this equation can be transformed into (cf. [11, 15, 3, 1])

$$\int_{\Omega} \delta \mathbf{u}^T [\mathbf{R}\ddot{\mathbf{u}}] d\Omega + \int_{\Omega} \delta \epsilon^T \sigma d\Omega = \int_{\Omega} \delta \mathbf{u}^T \mathbf{p} d\Omega + \int_{\partial\Omega_t} \delta \mathbf{u}^T \mathbf{t} d\Gamma \tag{2.12}$$

## 2.3 Finite element discretization of the IVP

For the use of implicit time integration scheme, Eq. 2.12 is considered to be valid at time $t+\Delta t$. The updated stress at global $(I+1)$-th iteration reads

$$\sigma_{t+\Delta t}^{(I+1)} = \sigma_t + \Delta\sigma_{t+\Delta t}^{(I+1)} = \sigma_{t+\Delta t}^{(I)} + d\sigma^{(I)} \tag{2.13}$$

in which the correction of the $(I)$-th incremental stress $d\sigma^{(I)}$ can be written as

$$d\sigma^{(I)} = \left(\frac{\partial\sigma}{\partial\epsilon}\right)_{t+\Delta t}^{(I)} d\epsilon^{(I)} = \mathbf{D}^{c,(I)} d\epsilon^{(I)} \tag{2.14}$$

Then the $(I+1)$-th iteration form of Eq. 2.12 can be expressed as

$$\int_{\Omega} \delta \mathbf{u}^T [\mathbf{R}\ddot{\mathbf{u}}_{t+\Delta t}^{(I+1)}] d\Omega + \int_{\Omega} \delta\epsilon^T d\sigma^{(I)} d\Omega = \int_{\Omega} \delta \mathbf{u}^T \mathbf{p}_{t+\Delta t}^{(I+1)} d\Omega$$
$$+ \int_{\partial\Omega_t} \delta \mathbf{u}^T \mathbf{t}_{t+\Delta t}^{(I+1)} d\Gamma - \int_{\Omega} \delta\epsilon^T \sigma_{t+\Delta t}^{(I)} d\Omega \tag{2.15}$$

Making use of the standard finite element formulation the continuous displacement field $\mathbf{u}$ and the continuous acceleration field $\ddot{\mathbf{u}}$ are discretized as

$$\mathbf{u}(\mathbf{x}, t) = \mathbf{H}(\mathbf{x})\mathbf{a}(t) \tag{2.16}$$

$$\ddot{\mathbf{u}}(\mathbf{x}, t) = \mathbf{H}(\mathbf{x})\ddot{\mathbf{a}}(t) \tag{2.17}$$

$$\dot{\epsilon}(\mathbf{x}, t) = \mathbf{B}(\mathbf{x})\dot{\mathbf{a}}(t) = \mathbf{L}\mathbf{H}\dot{\mathbf{a}}(t) \tag{2.18}$$

where $\mathbf{H}(\mathbf{x})$, $\mathbf{B}(\mathbf{x})$ the interpolation matrix and the strain-nodal displacement matrix.

Substitution of Eqs. 2.16 to 2.18 and 2.14 into Eq. 2.15 leads to

$$\delta\mathbf{a}^T \int_{\Omega} \mathbf{H}^T \mathbf{R}\mathbf{H}\ddot{\mathbf{a}}_{t+\Delta t}^{(I+1)} d\Omega + \delta\mathbf{a}^T \int_{\Omega} \mathbf{B}^T \mathbf{D}^{c,(I)} \mathbf{B} d\mathbf{a}^{(I)} d\Omega = \delta\mathbf{a}^T \int_{\Omega} \mathbf{H}^T \mathbf{p}_{t+\Delta t}^{(I+1)} d\Omega$$
$$+ \delta\mathbf{a}^T \int_{\partial\Omega_t} \mathbf{H}^T \mathbf{t}_{t+\Delta t}^{(I+1)} d\Gamma - \delta\mathbf{a}^T \int_{\Omega} \mathbf{B}^T \sigma_{t+\Delta t}^{(I)} d\Omega \tag{2.19}$$

Because this identity must hold for any admissible $\delta\mathbf{a}$ we obtain

$$\mathbf{M}\ddot{\mathbf{a}}^{(I+1)} + \mathbf{K}^{(I)}d\mathbf{a}^{(I)} = \mathbf{f}_{ext}^{(I+1)} - \mathbf{f}_{int}^{(I)} \tag{2.20}$$

where the subscript t+$\Delta$t is dropped for simplicity. The mass matrix $\mathbf{M}$, the stiffness matrix $\mathbf{K}^{(I)}$, the internal force vector $\mathbf{f}_{int}^{(I)}$ and the external load vector $\mathbf{f}_{ext}^{(I+1)}$ are given by

$$\mathbf{M} = \int_{\Omega} \mathbf{H}^T \mathbf{R} \mathbf{H} d\Omega \qquad\qquad \mathbf{K}^{(I)} = \int_{\Omega} \mathbf{B}^T \mathbf{D}^{c,(I)} \mathbf{B} d\Omega$$

$$\mathbf{f}_{int}^{(I)} = \int_{\Omega} \mathbf{B}^T \sigma_{t+\Delta t}^{(I)} d\Omega \qquad \mathbf{f}_{ext}^{(I+1)} = \int_{\Omega} \mathbf{H}^T \mathbf{p}_{t+\Delta t}^{(I+1)} d\Omega + \int_{\partial\Omega_t} \mathbf{H}^T \mathbf{t}_{t+\Delta t}^{(I+1)} d\Gamma \tag{2.21}$$

Eq. 2.20 represents the semi-discrete nonlinear equation of motion governing the response of a system of finite elements.

## 2.4    Time integration scheme

After spatial integration of the virtual work equation we apply the direct integration method to obtain a full discrete equation of motion. A one step time integration scheme of Newmark family is used in this report, in which quadratic expansion is used

$$\mathbf{a}_{t+\Delta t} = \mathbf{a}_t + \dot{\mathbf{a}}_t \Delta t + [(\frac{1}{2} - \beta)\ddot{\mathbf{a}}_t + \beta\ddot{\mathbf{a}}_{t+\Delta t}]\Delta t^2 \tag{2.22}$$

$$\dot{\mathbf{a}}_{t+\Delta t} = \dot{\mathbf{a}}_t + [(1-\gamma)\ddot{\mathbf{a}}_t + \gamma\ddot{\mathbf{a}}_{t+\Delta t}]\Delta t \tag{2.23}$$

We use $(\beta,\gamma) = (\frac{1}{4}, \frac{1}{2})$ for all calculations performed in this report, which is called the average acceleration method or trapezoidal rule. We can rewrite Eq. 2.22 as

$$\ddot{\mathbf{a}}_{t+\Delta t}^{(I+1)} = c_0\Delta\mathbf{a}^{(I+1)} - c_1\dot{\mathbf{a}}_t - c_2\ddot{\mathbf{a}}_t \tag{2.24}$$

where the coefficients are given by

$$c_0 = \frac{1}{\beta\Delta t^2} \qquad\qquad c_1 = \frac{1}{\beta\Delta t} \qquad\qquad c_2 = \frac{1}{2\beta} - 1 \tag{2.25}$$

The (I+1)-th incremental displacement can generally be expressed as

$$\Delta\mathbf{a}^{(I+1)} = \Delta\mathbf{a}^{(I)} + d\mathbf{a}^{(I)} \tag{2.26}$$

Then we obtain

$$\ddot{\mathbf{a}}_{t+\Delta t}^{(I+1)} = c_0 d\mathbf{a}^{(I)} + c_0\Delta\mathbf{a}^{(I)} - c_1\dot{\mathbf{a}}_t - c_2\ddot{\mathbf{a}}_t = c_0 d\mathbf{a}^{(I)} + \ddot{\mathbf{a}}_{t+\Delta t}^{(I)} \tag{2.27}$$

Substitution of Eq. 2.27 into Eq. 2.20 leads to the following system of equations

$$\hat{\mathbf{K}}^{(I)}d\mathbf{a}^{(I)} = \hat{\mathbf{f}}^{(I+1)} \tag{2.28}$$

where the dynamic tangent matrix $\hat{\mathbf{K}}^{(I)}$ and the effective load vector $\hat{\mathbf{f}}^{(I+1)}$ are defined as

$$\hat{\mathbf{K}}^{(I)} = \mathbf{K}^{(I)} + c_0\mathbf{M} \tag{2.29}$$

$$\hat{\mathbf{f}}^{(I+1)} = \mathbf{f}_{ext}^{(I+1)} - \mathbf{f}_{int}^{(I)} - \mathbf{M}\ddot{\mathbf{a}}_{t+\Delta t}^{(I)} \tag{2.30}$$

respectively.

The algorithm for implicit integration of the semi-discrete equation of motion is outlined in Table 2.1. This scheme corresponds to a full Newton-Raphson scheme where the tangential stress-strain matrix $\mathbf{D}^{c,(I)}$ is updated at each iteration.

1. calculate constants

$$c_0 = \frac{1}{\beta \Delta t^2} \qquad c_1 = \frac{1}{\beta \Delta t} \qquad c_2 = \frac{1}{2\beta} - 1 \qquad c_3 = (1 - \gamma)\Delta t \qquad c_4 = \gamma \Delta t$$

2. initialize $\mathbf{a}(0), \qquad \dot{\mathbf{a}}(0), \qquad \ddot{\mathbf{a}}(0), \qquad t = 0 \text{ s}$

3. initialize $\Delta \mathbf{a}^{(0)}, \qquad \mathbf{K}^{(0)}, \qquad \hat{\mathbf{K}}^{(0)}, \qquad \mathbf{f}_{ext}^{(1)}, \qquad \mathbf{f}_{int}^{(0)}, \qquad \hat{\mathbf{f}}^{(1)}$

4. solve for the delta-incremental displacements

$$\hat{\mathbf{K}}^{(I)} \mathbf{da}^{(I)} = \hat{\mathbf{f}}^{(I+1)}$$

5. update the iterative incremental displacements, accelerations, velocities and displacements

$$\Delta \mathbf{a}_{t+\Delta t}^{(I+1)}, \qquad \ddot{\mathbf{a}}_{t+\Delta t}^{(I+1)}, \qquad \dot{\mathbf{a}}_{t+\Delta t}^{(I+1)}, \qquad \mathbf{a}_{t+\Delta t}^{(I+1)}$$

6. check convergence criterion, if not converged: $I \longleftarrow I+1$

   update $\mathbf{K}^{(I)}, \qquad \hat{\mathbf{K}}^{(I)}, \qquad \mathbf{f}_{ext}^{(I+1)}, \qquad \mathbf{f}_{int}^{(I)}, \qquad \hat{\mathbf{f}}^{(I+1)}$ . Go to 4.

7. set new accelerations, velocities and displacements.

$$[\mathbf{a}_{t+\Delta t}, \dot{\mathbf{a}}_{t+\Delta t}, \ddot{\mathbf{a}}_{t+\Delta t}] = [\mathbf{a}_{t+\Delta t}^{(I+1)}, \dot{\mathbf{a}}_{t+\Delta t}^{(I+1)}, \ddot{\mathbf{a}}_{t+\Delta t}^{(I+1)}]$$

Table 2.1: Global implicit integration procedure

# Chapter 3

# Constitutive models

In this Chapter, the material models used to describe the mechanical response of concrete are discussed. The corresponding algorithmic treatments are also given for implementation in a finite element programme.

## 3.1 Plasticity model

Plasticity models with an appropriate yield function and flow rule can be used to describe mechanical behavior of concrete under compressive loading and tensile loading. For example, the yield functions of Von Mises and Drucker-Prager can be used for model-II dominated failure problems. On the other hand the Rankine criterion is suited to predict a mode-I failure pattern.

We will use three plasticity models in the simulations, namely the standard Von Mises plastic model, Perzyna viscoplastic model and Duvaut-Lions viscoplastic model. As illustrated in Chapter 1, the rate dependence of plastic flow characterizing the latter two models implicitly introduces an internal length scale in the constitutive descriptions and preserves the well-posedness of the IVP upon the onset of strain softening.

### 3.1.1 Standard plasticity model

In the flow theory of plasticity, the material behavior can be written in a general rate format

$$\dot{\epsilon} = \dot{\epsilon}_e + \dot{\epsilon}_p \tag{3.1}$$

$$\dot{\sigma} = \mathbf{D}^e(\dot{\epsilon} - \dot{\epsilon}_p) = \mathbf{D}^e \dot{\epsilon}_e \tag{3.2}$$

$$\dot{\epsilon}_p = \dot{\lambda}\mathbf{m} \tag{3.3}$$

where $\mathbf{D}^e$ is the elastic stiffness tensor, $\dot{\lambda}$ is the plastic multiplier and $\mathbf{m}$ is the direction of plastic flow.

Loading and unloading conditions can be conveniently expressed by Kuhn-Tucker conditions

$$f \leq 0, \qquad \dot{\lambda} \geq 0, \qquad f\dot{\lambda} = 0 \tag{3.4}$$

where $f(\sigma, \kappa)$ is the yield function with a number of internal variables collected in a vector $\kappa$ which describe the plastic strain history.

For isotropic hardening/softening this vector reduces to a scalar-valued hardening/softening parameter $\kappa$ depending on strain history through invariant measures of the plastic strain $\epsilon_p$. According to the strain hardening hypothesis

$$\dot{\kappa} = \sqrt{2/3(\dot{\epsilon}_p)^T \mathbf{Q} \dot{\epsilon}_p} \tag{3.5}$$

where $\mathbf{Q} = \text{diag}[1,1,1,1/2,1/2,1/2]$. This definition of $\kappa$ is used in this report.

7

We make use of a Von Mises yield function which is described as

$$f(\sigma, \kappa) = \sqrt{3J_2} - \bar{\sigma}(\kappa) \tag{3.6}$$

where $J_2$ is the second invariant of the deviatoric stress. The combination of flow theory of plasticity with Von Mises yield contour is also named the $J_2$-flow theory.

The isotropic softening laws have been utilized,

- the *linear softening law*

$$\bar{\sigma}(\kappa) = \begin{cases} E_n \kappa + \bar{\sigma}_0 & 0 \leq \kappa \leq \kappa_u \\ 0 & \kappa > \kappa_u \end{cases} \tag{3.7}$$

where $E_n$ is the softening modulus, $\bar{\sigma}_0$ the initial yield stress and $\kappa_u$ the ultimate value of $\kappa$ at which $\bar{\sigma}$ has reduced to zero;

- the *exponential softening law*

$$\bar{\sigma}(\kappa) = \bar{\sigma}_\infty + (\bar{\sigma}_0 - \bar{\sigma}_\infty)e^{(-\beta\kappa)} \tag{3.8}$$

where $\bar{\sigma}_\infty$ is the yield stress at infinite value of $\kappa$.

Another condition for plastic straining is

$$\dot{f} = 0 \tag{3.9}$$

which is usually called Prager's consistency condition.

On the material (local) level, the constitutive rate equation should be integrated to calculate the stress $\sigma_{t+\Delta t}$ at time $t+\Delta t$ and to provide the tangential material stiffness matrix (cf. [3]). This is achieved by utilizing the fully implicit Euler Backward integration scheme, i.e. the closest point projection algorithm.

The incremental form of constitutive equation Eq. 3.1 to Eq. 3.3 is

$$\sigma_{t+\Delta t} = \sigma_t + \Delta\sigma \tag{3.10}$$

$$\Delta\sigma = \mathbf{D}^e(\Delta\epsilon - \Delta\epsilon_p) \tag{3.11}$$

$$\Delta\epsilon_p = \Delta\lambda \mathbf{m}_{t+\Delta t} \tag{3.12}$$

We cast Eq. 3.10 to Eq. 3.12 in the form

$$\mathbf{g}(\sigma_{t+\Delta t}, \lambda_{t+\Delta t}) = \mathbf{0} \tag{3.13}$$

where

$$\mathbf{g}(\sigma_{t+\Delta t}, \lambda_{t+\Delta t}) = \sigma_{t+\Delta t} - \mathbf{D}^e \epsilon_{t+\Delta t} + \Delta\lambda \mathbf{D}^e \mathbf{m}_{t+\Delta t} \tag{3.14}$$

To determine $\sigma_{t+\Delta t}$ and $\Delta\lambda$ we must augment Eqs. 3.13 by the requirement that the yield condition is complied with at the end of a loading step

$$f(\sigma_{t+\Delta t}, \kappa_{t+\Delta t}) = f(\sigma_{t+\Delta t}, \lambda_{t+\Delta t}) = 0 \tag{3.15}$$

A Newton-Raphson procedure is set up at integration point level to solve this nonlinear system of equations

$$\begin{bmatrix} \sigma_{t+\Delta t}^{k+1} \\ \lambda_{t+\Delta t}^{k+1} \end{bmatrix} = \begin{bmatrix} \sigma_{t+\Delta t}^{k} \\ \lambda_{t+\Delta t}^{k} \end{bmatrix} - \begin{bmatrix} \frac{\partial \mathbf{g}}{\partial \sigma} & \frac{\partial \mathbf{g}}{\partial \lambda} \\ \frac{\partial f}{\partial \sigma} & \frac{\partial f}{\partial \lambda} \end{bmatrix}^{-1} \begin{bmatrix} \mathbf{g}(\sigma_{t+\Delta t}^{k}, \lambda_{t+\Delta t}^{k}) \\ f(\sigma_{t+\Delta t}^{k}, \lambda_{t+\Delta t}^{k}) \end{bmatrix} \tag{3.16}$$

where k is the iteration counter of the local Newton-Raphson iteration. In view of Eq. 3.14 the differentials in Eq. 3.16 can be elaborated as

$$\frac{\partial \mathbf{g}}{\partial \boldsymbol{\sigma}} = \mathbf{A} = \mathbf{I} + \Delta\lambda \mathbf{D}^e \frac{\partial \mathbf{m}}{\partial \boldsymbol{\sigma}} \tag{3.17}$$

$$\frac{\partial \mathbf{g}}{\partial \lambda} = \mathbf{D}^e \bar{\mathbf{m}} = \mathbf{D}^e(\mathbf{m} + \Delta\lambda \frac{\partial \mathbf{m}}{\partial \kappa}\frac{\partial \kappa}{\partial \lambda}) = \mathbf{D}^e(\mathbf{m} + \Delta\lambda \frac{\partial \kappa}{\partial \lambda}\frac{\partial \mathbf{m}}{\partial \kappa}) \tag{3.18}$$

A consistent linearization of Eq. 3.10 to Eq. 3.12 together with consistency condition Eq. 3.9 leads to the algorithmic tangential stiffness relation

$$\dot{\boldsymbol{\sigma}} = \mathbf{D}^{ep}\dot{\boldsymbol{\epsilon}} = \left[\mathbf{U} - \frac{\mathbf{U}\bar{\mathbf{m}}\mathbf{n}^T\mathbf{U}}{h + \mathbf{n}^T\mathbf{U}\bar{\mathbf{m}}}\right]\dot{\boldsymbol{\epsilon}} \tag{3.19}$$

where $\mathbf{U} = \mathbf{A}^{-1}\mathbf{D}^e$, $h = -\frac{\partial f}{\partial \kappa}\frac{\kappa}{\lambda}$ and $\mathbf{n} = \frac{\partial f}{\partial \boldsymbol{\sigma}}$.

### 3.1.2   Perzyna viscoplastic model

In the viscoplastic model according to Perzyna ([10]) the viscoplastic strain rate is defined similar to the plastic strain rate in standard plasticity (i.e. Eq. 3.1 and Eq. 3.2) with a modified definition of the plastic multiplier.

$$\dot{\boldsymbol{\epsilon}} = \dot{\lambda}\mathbf{m} \tag{3.20}$$

$$\dot{\lambda} = \eta\phi(f) \tag{3.21}$$

in which $\eta$ is the viscosity parameter, $\phi$ is an arbitrary function of the yield function for which we take a power law expression according to (cf. [11, 15])

$$\phi(f) = \left[\left\langle \frac{f}{\bar{\sigma}_0} \right\rangle\right]^N \tag{3.22}$$

with N a constant, $\bar{\sigma}_0$ the initial yield stress and $\left\langle \frac{f}{\bar{\sigma}_0} \right\rangle = \frac{f/\bar{\sigma}_0 + |f/\bar{\sigma}_0|}{2}$.

A full implicit integration scheme is used to obtain the stress $\boldsymbol{\sigma}_{t+\Delta t}$ at time t+$\Delta$t and the consistent tangential stiffness matrix $\mathbf{D}^{vp}$. The same incremental form of constitutive equations as Eq. 3.10 to Eq. 3.12 can be obtained, then we obtain the following equations

$$r = \phi(\boldsymbol{\sigma}_{t+\Delta t}, \lambda_{t+\Delta t}) - \frac{\Delta\lambda}{\eta\Delta t} = 0 \tag{3.23}$$

$$\Delta\boldsymbol{\sigma} = \mathbf{D}^e[\Delta\boldsymbol{\epsilon} - \Delta\lambda\mathbf{m}_{t+\Delta t}] \tag{3.24}$$

A local Newton-Raphson procedure is applied to compute $\Delta\lambda$ and $\Delta\boldsymbol{\sigma}$. During the linearization a consistent tangent stiffness matrix is obtained

$$\mathbf{D}^{vp} = \mathbf{P} - \frac{1}{\alpha}\mathbf{P}\left[\mathbf{m} + \Delta\lambda\frac{\partial \mathbf{m}}{\partial \lambda}\right]\left[\frac{\partial \phi}{\partial \boldsymbol{\sigma}}\right]^T\mathbf{P} \tag{3.25}$$

in which

$$\mathbf{P} = \left[(\mathbf{D}^e)^{-1} + \Delta\lambda\frac{\partial \mathbf{m}}{\partial \boldsymbol{\sigma}}\right]^{-1} \tag{3.26}$$

$$\alpha = \left[\frac{\partial \phi}{\partial \boldsymbol{\sigma}}\right]^T\mathbf{P}\left[\mathbf{m} + \Delta\lambda\frac{\partial \mathbf{m}}{\partial \lambda}\right] + \frac{1}{\eta\Delta t} - \frac{\partial \phi}{\partial \lambda} \tag{3.27}$$

Algorithmic treatment for Perzyna viscoplastic model is outlined in Table 3.1.

1. update strain increment and total strain $\Delta\epsilon$, $\epsilon$

2. compute trial stress $\sigma^{tr} = \mathbf{D}^e(\epsilon - \epsilon_{vp}^t)$

3. if $f(\sigma^{tr}, \kappa_t) \geq 0$ : plastic state

        (1) initialize $\Delta\lambda^{(0)} = 0$, $\Delta\sigma^{(0)} = 0$

        (2) perform local interation

        (3) update $\Delta\lambda$, $\Delta\sigma$, $\sigma_{t+\Delta t}$, $\mathbf{D}^{vp}$

        (4) check convergence, if not convergenced go to (2)

4. else: elastic state, $\sigma_{t+\Delta t} = \sigma^{tr}$

Table 3.1: Updating the stress and strain for Perzyna model

### 3.1.3  Duvaut-Lions viscoplastic model

The viscoplastic model proposed by Duvaut and Lions ([4]) is in its elaboration closer connected to rate independent plasticity. This model is based on the difference in response between the rate independent material and the viscoplastic material. Thus the model has the advantage that it can be combined with a yield surface which has an apex or which is non-smooth. The viscoplastic strain rate and hardening rate are defined as

$$\dot{\epsilon}_{vp} = \frac{1}{\tau}[\mathbf{D}^e]^{-1}(\sigma - \sigma_p) \tag{3.28}$$

$$\dot{\kappa} = -\frac{1}{\tau}(\kappa - \kappa_p) \tag{3.29}$$

where subscript p denotes the contribution of the rate independent material and $\tau$ is the relaxation time of the material and, in general, is strain and strain rate dependent.

The stain rate decomposition (i.e. Eq. 3.1 and Eq. 3.2) is still used.

A two-step integration scheme is used to determine the quantities $\sigma_p$, $\kappa_p$, $\sigma$ and consistent tangent stiffness matrix $\mathbf{D}^{vp}$ (cf. [11, 15]).

- **STEP1**: we apply the fully implicit Euler Backward method introduced in section 3.1.1 to integrate the backbone model to determine $\sigma_p$ , $\kappa_p$ and the tangential stiffness relation (cf. 3.19)

$$\Delta\sigma_p = \mathbf{D}^{ep}\Delta\epsilon \tag{3.30}$$

- **STEP2**: A generalized Euler method is used to estimate the incremental viscoplastic strain

$$\Delta\epsilon_{vp} = \left[\dot{\epsilon}_{vp}^t(1 - \theta) + \theta\dot{\epsilon}_{vp}^{t+\Delta t}\right]\Delta t \tag{3.31}$$

where $\theta$ is the interpolation parameter for which $0 \leq \theta \leq 1$.

Utilizing the incremental form relations Eq. 3.10, Eq. 3.11 and Eq. 3.28 for $\dot{\epsilon}_{vp}^{t+\Delta t}$ stress update and material tangent stiffness matrix can be obtained

$$\Delta\sigma = \mathbf{D}^{vp}\Delta\epsilon - \Delta\mathbf{q} \tag{3.32}$$

1. update strain increment and total strain $\Delta\epsilon$, $\epsilon$

2. compute trial stress $\sigma^{tr} = \mathbf{D}^e(\epsilon - \epsilon^t_{vp})$

3. if $f(\sigma^{tr}, \kappa^t) \geq 0$ : plastic state

        (1) calculate $\sigma^{t+\Delta t}_p$, $\kappa^{t+\Delta t}_p$, $\mathbf{D}^{ep}$

        (2) calculate $\Delta\sigma$, $\sigma^{t+\Delta t}$, $\kappa^{t+\Delta t}$, $\sigma^{t+\Delta t}_{vp}$, $\dot{\epsilon}^{t+\Delta t}_{vp}$, $\mathbf{D}^{vp}$

4. if $f(\sigma^{tr}, \kappa^t) < 0$: $\sigma^{t+\Delta t} = \sigma^{tr}$

Table 3.2: Updating the stress and strain for Duvaut-Lions model

$$\mathbf{D}^{vp} = \frac{\tau}{\tau + \theta\Delta t}\left[\mathbf{D}^e + \frac{\theta\Delta t}{\tau}\mathbf{D}^{ep}\right] \tag{3.33}$$

$$\Delta\mathbf{q} = \frac{\tau\Delta t}{\tau + \theta\Delta t}\left[(1-\theta)\mathbf{D}^e\dot{\epsilon}^t_{vp} + \frac{\theta}{\tau}\sigma^t_{vp}\right] \tag{3.34}$$

where $\Delta\mathbf{q}$ is an extra pseudo-nodal force in equation of motion. $\sigma^t_{vp} = \sigma^t - \sigma^t_p$ is the viscous stress at the beginning of the time step.

In Table 3.2 the algorithm for Duvaut-Lions model is outlined. The update of $\kappa$ at time t+$\Delta$t can be performed by using

$$\kappa^{t+\Delta t} = \kappa^t e^{-\Delta t/\tau} + (1 - e^{-\Delta t/\tau})\kappa_p \tag{3.35}$$

Note that in the Duvaut-Lions model, the loading and unloading condition is determined by the total stress state. In case unloading happens in the back-bone stress update while the total stress state is still outside the inviscid yield surface, a modification should be adopted. The Kuhn-Tucker conditions in back-bone model (i.e. Eq. 3.4) are modified as

$$f \leq 0, \qquad f\dot{\lambda} = 0 \tag{3.36}$$

A negative value of $\dot{\lambda}$ is allowed.

The maximum principal stress model of Rankine is used for Duvaut-Lions viscoplasticity

$$f(\sigma, \kappa) = \sigma_i - \bar{\sigma}(\kappa) \tag{3.37}$$

in which $\sigma_i = \max(\sigma_1, \sigma_2, \sigma_3)$. Considering a plane stress condition, we have

$$f(\sigma, \kappa) = \frac{1}{2}(\sigma_x + \sigma_y) + \sqrt{\frac{1}{4}(\sigma_x + \sigma_y)^2 + \tau^2_{xy}} - \bar{\sigma}(\kappa) \tag{3.38}$$

There is an apex in the Rankine yield contour, which has been treated by Feenstra, Pamin and Meschke (cf. [5, 8, 7]). Due to the used loading condition (i.e. one-directional monotonic loading) the apex issue is not treated in the simulation.

## 3.2   Continuum damage model

The continuum damage model describes changes at the microstructual level in the material via a finite number of scalar or tensor-valued internal variables. In this report, an isotropic elasticity based damage

model with a single scalar-valued damage variable is used,

$$\sigma = (1 - \omega)\mathbf{D}^e\epsilon \qquad , \qquad 0 \leq \omega \leq 1 \tag{3.39}$$

where $\omega$ is a scalar damage parameter. It is a function of history parameters and its evolution is controlled by a loading function.

In the local formulation of the damage model, the damage parameter $\omega$, history parameter $\kappa$ and loading function can be defined as

$$\omega = \omega(\kappa) \tag{3.40}$$

$$\kappa = max(\epsilon_{eq}, \kappa_i) \tag{3.41}$$

$$f(\epsilon_{eq}, \kappa) = \epsilon_{eq} - \kappa \tag{3.42}$$

where the equivalent strain $\epsilon_{eq}$ is an invariant measure of strain, $\kappa_i$ is the threshold of damage initiation.

Similar to the standard plasticity theory the loading-unloading condition can be formulated as Kuhn-Tucker conditions

$$f \leq 0 \quad , \qquad \dot{\kappa} \geq 0 \quad , \qquad f\dot{\kappa} = 0 \tag{3.43}$$

Just as the standard plastic model combined with strain softening law, at a certain stage of damage evolution, the continuum damage model ceases to produce meaningful results. The governing equations of motion become elliptic and the IVP becomes ill-posed.

Nonlocal and gradient enhancedment have the regularizing effect to the continuum damage model. The constant gradient damage (CGD) model and the strain-based transient-gradient damage model (STGD) will be adopted in this report.

### 3.2.1 Implicit constant gradient damage model

In the nonlocal formulation of the constitutive model the nonlocal conterpart $\bar{\chi}$ of a local state variable $\chi$ over the surrounding domain $\Omega$ with respect to the weight function G is given by (cf. [9, 2, 1])

$$\bar{\chi}(\mathbf{x}) = \frac{\int_\Omega G(\boldsymbol{\xi})\chi(\mathbf{x} + \boldsymbol{\xi})d\Omega(\boldsymbol{\xi})}{\int_\Omega G(\boldsymbol{\xi})d\Omega(\boldsymbol{\xi})} \tag{3.44}$$

with $\boldsymbol{\xi}$ a vector pointing to the infinitesimal volume.

Nonlocal constitutive relations can be considered as a point of departure for constructing a gradient model. The local quantity $\chi(\mathbf{x})$ can be developed into a Taylor series around $\mathbf{x}$ and substituted into Eq. 3.44, under the assumption of isotropy, a new expresssion for $\bar{\chi}$ is found

$$\bar{\chi}(\mathbf{x}) = \chi(\mathbf{x}) + C_2\nabla^2\chi(\mathbf{x}) + C_4\nabla^4\chi(\mathbf{x}) + \ldots \tag{3.45}$$

where $\nabla = [\partial/\partial x, \ \partial/\partial y, \ \partial/\partial z]^T$. This series is called the explicit gradient enhancement.

An alternative gradient formulation can be derived from Eq. 3.45 by applying the Laplacian operator to it and multiplying by $C_2$. The result is substracted from Eq. 3.45 , which gives

$$\bar{\chi}(\mathbf{x}) - C_2\nabla^2\bar{\chi}(\mathbf{x}) = \chi(\mathbf{x}) + (C_4 - C_2{}^2)\nabla^4\chi(\mathbf{x}) + (C_6 - C_2C_4)\nabla^6\chi(\mathbf{x}) + \ldots \tag{3.46}$$

This series is called implicit-gradient enhancement. The same procedure as above can be repeated to derive higher-order implicit gradient-enhancement.

The parameters $C_2, C_4, \ldots$ depend on the weight function G.

It has been proved that implicit formulations show better performance than explicit formulations. Considering the equivalent strain $\epsilon_{eq}(\mathbf{x})$ as the local state variable, the second-order implicit gradient-enhancement can be formulated as

$$\bar{\epsilon}_{eq}(\mathbf{x}) - c\nabla^2\bar{\epsilon}_{eq}(\mathbf{x}) = \epsilon_{eq}(\mathbf{x}) \tag{3.47}$$

where the gradient parameter c has the dimension of length squared. We adopt the phenomenological view that c reflects the length scale of the failure process that we wish to describe macroscopically.

Higher-order continuum requires additional boundary conditions, either of the Dirichlet ($\bar{\epsilon}_{eq} = \hat{\epsilon}$) or of the Neumann type ($\mathbf{n}^T \nabla \bar{\epsilon}_{eq} = \hat{\epsilon}_n$). The natural boundary condition

$$\mathbf{n}^T \nabla \bar{\epsilon}_{eq} = 0 \tag{3.48}$$

where $\mathbf{n}$ is the outward normal to the boundary, is used in the simulations.

Now the gradient enhanced damage constitutive relation can be written as

$$\sigma = (1 - \omega)\mathbf{D}^e \epsilon \qquad , \qquad 0 \leq \omega \leq 1 \tag{3.49}$$

$$\omega = \omega(\kappa) \tag{3.50}$$

$$\kappa = max(\bar{\epsilon}_{eq}, \kappa_i) \tag{3.51}$$

$$f(\bar{\epsilon}_{eq}, \kappa) = \bar{\epsilon}_{eq} - \kappa \tag{3.52}$$

$$f \leq 0 \quad , \qquad \dot{\kappa} \geq 0 \quad , \qquad f\dot{\kappa} = 0 \tag{3.53}$$

The nonlocal equivalent strain $\bar{\epsilon}_{eq}$ is defined through Eq. 3.47

We adopt two damage evolution laws, namely

- the *linear softening* damage evolution law

$$\omega(\kappa) = 1 - \frac{\kappa_i}{\kappa} \frac{\kappa_c - \kappa}{\kappa_c - \kappa_i} \tag{3.54}$$

characterized in the one-dimensional situation by a linear decrease of stress until a zero-stress level is reached for the ultimate strain $\kappa_c$;

- the *exponential softening* damage evolution law

$$\omega(\kappa) = 1 - \frac{\kappa_i}{\kappa} \left[ (1 - \alpha) + \alpha e^{[-\beta(\kappa - \kappa_i)]} \right] \tag{3.55}$$

where $\alpha$ and $\beta$ are constant parameters,

and the modified Von Mises definition of equivalent strain

$$\epsilon_{eq} = \frac{(k-1)I_1}{2k(1-2\nu)} + \frac{1}{2k} \sqrt{\frac{(k-1)^2 I_1^2}{(1-2\nu)^2} + \frac{2kJ_2}{(1+\nu)^2}} \tag{3.56}$$

where $I_1$ the first invariant of strain tensor, $J_2$ the second invariant of the deviatoric strain tensor and k the ratio between uniaxial compression yield stress and uniaxial tension yield stress.

In section 2.2 we have derived a weak form of the initial value problem. The (I+1)-th iteration form at time t+$\Delta$t is

$$\int_\Omega \delta \mathbf{u}^T [\mathbf{R} \ddot{\mathbf{u}}_{t+\Delta t}^{(I+1)}] d\Omega + \int_\Omega \delta \epsilon^T d\sigma^{(I)} d\Omega = \int_\Omega \delta \mathbf{u}^T \mathbf{p}_{t+\Delta t}^{(I+1)} d\Omega$$
$$+ \int_{\partial \Omega_t} \delta \mathbf{u}^T \mathbf{t}_{t+\Delta t}^{(I+1)} d\Gamma - \int_\Omega \delta \epsilon^T \sigma_{t+\Delta t}^{(I)} d\Omega \tag{3.57}$$

Similarly, the weak form of the modified Helmholtz equation Eq. 3.47 can be formed

$$\int_\Omega \delta \bar{\epsilon}_{eq}(\bar{\epsilon}_{eq} - c\nabla^2 \bar{\epsilon}_{eq}) d\Omega = \int_\Omega \delta \bar{\epsilon}_{eq} \epsilon_{eq} d\Omega \tag{3.58}$$

14

Using Green's formula of integration by parts and considering boundary condition Eq. 3.48, the weak form of the diffusion equation results in

$$\int_\Omega \delta\bar{\epsilon}_{eq}\bar{\epsilon}_{eq}d\Omega + \int_\Omega \nabla\delta\bar{\epsilon}_{eq}^T c\nabla\bar{\epsilon}_{eq}d\Omega = \int_\Omega \delta\bar{\epsilon}_{eq}\epsilon_{eq}d\Omega \qquad (3.59)$$

The (I+1)-th iteration form at time $t+\Delta t$ can be written as

$$\int_\Omega \left[\delta\bar{\epsilon}_{eq}d\bar{\epsilon}_{eq,t+\Delta t}^{(I)} + \nabla\delta\bar{\epsilon}_{eq}^T c\nabla d\bar{\epsilon}_{eq,t+\Delta t}^{(I)}\right]d\Omega - \int_\Omega \delta\bar{\epsilon}_{eq}d\epsilon_{eq,t+\Delta t}^{(I)}d\Omega = \int_\Omega \delta\bar{\epsilon}_{eq}\epsilon_{eq,t+\Delta t}^{(I)}d\Omega$$
$$-\int_\Omega \left[\delta\bar{\epsilon}_{eq}\bar{\epsilon}_{eq,t+\Delta t}^{(I)} + \nabla\delta\bar{\epsilon}_{eq}^T c\nabla\bar{\epsilon}_{eq,t+\Delta t}^{(I)}\right]d\Omega \qquad (3.60)$$

where we have introduced the decompositions

$$\bar{\epsilon}_{eq,t+\Delta t}^{(I+1)} = \bar{\epsilon}_{eq,t+\Delta t}^{(I)} + d\bar{\epsilon}_{eq,t+\Delta t}^{(I)} \qquad (3.61)$$

$$\epsilon_{eq,t+\Delta t}^{(I+1)} = \epsilon_{eq,t+\Delta t}^{(I)} + d\epsilon_{eq,t+\Delta t}^{(I)} \qquad (3.62)$$

Quantities $d\sigma^{(I)}$ and $d\epsilon_{eq}{}^{(I)}$ can be expressed as

$$d\sigma^{(I)} = (1-\omega^{(I)})\mathbf{D}^e\left[\frac{\partial\epsilon}{\partial\mathbf{u}}\right]^T d\mathbf{u}^{(I)} - \mathbf{D}^e\epsilon^{(I)}\left(\frac{\partial\omega}{\partial\kappa}\right)^{(I)}\left(\frac{\partial\kappa}{\partial\bar{\epsilon}_{eq}}\right)^{(I)}d\bar{\epsilon}_{eq}^{(I)} \qquad (3.63)$$

$$d\epsilon_{eq}^{(I)} = \left[\left(\frac{\partial\epsilon_{eq}}{\partial\epsilon}\right)^{(I)}\right]^T\left[\frac{\partial\epsilon}{\partial\mathbf{u}}\right]^T d\mathbf{u}^{(I)} \qquad (3.64)$$

where subscript $t+\Delta t$ is dropped for simplicity. In Eq. 3.63 , $\frac{\partial\kappa}{\partial\bar{\epsilon}_{eq}} = 1$ for loading and $\frac{\partial\kappa}{\partial\bar{\epsilon}_{eq}} = 0$ otherwise.

For the finite element implementation, a two-field discretization is used

$$\mathbf{u}(\mathbf{x},t) = \mathbf{H}_u(\mathbf{x})\mathbf{a}(t) \qquad (3.65)$$

$$\ddot{\mathbf{u}}(\mathbf{x},t) = \mathbf{H}_u(\mathbf{x})\ddot{\mathbf{a}}(t) \qquad (3.66)$$

$$\dot{\epsilon}(\mathbf{x},t) = \mathbf{B}_u(\mathbf{x})\dot{\mathbf{a}}(t) = \mathbf{L}\mathbf{H}_u\dot{\mathbf{a}}(t) \qquad (3.67)$$

$$\bar{\epsilon}_{eq}(\mathbf{x},t) = \mathbf{H}_\epsilon(\mathbf{x})\Lambda(t) \qquad (3.68)$$

$$\nabla\bar{\epsilon}_{eq}(\mathbf{x},t) = \mathbf{B}_\epsilon\Lambda(t) = \nabla\mathbf{H}_\epsilon(\mathbf{x})\Lambda(t) \qquad (3.69)$$

where $\mathbf{a}(t)$ and $\Lambda(t)$ contain the assembled nodal values of the nodal unknowns, the displacements and the nonlocal equivalent strains.

Substitution of Eqs. 3.63 to 3.69 into the weak forms of the field equations 3.57 and 3.60 yields

$$\delta\mathbf{a}^T\mathbf{M}^{(I)}\ddot{\mathbf{a}}^{(I+1)} + \delta\mathbf{a}^T\mathbf{K}_{uu}^{(I)}d\mathbf{a}^{(I)} + \delta\mathbf{a}^T\mathbf{K}_{u\epsilon}^{(I)}d\Lambda^{(I)} = \delta\mathbf{a}^T\mathbf{f}_{ext,u}^{(I+1)} - \delta\mathbf{a}^T\mathbf{f}_{int,u}^{(I)} \qquad (3.70)$$

$$\delta\Lambda^T\mathbf{K}_{\epsilon u}^{(I)}d\mathbf{a}^{(I)} + \delta\Lambda^T\mathbf{K}_{\epsilon\epsilon}^{(I)}d\Lambda^{(I)} = -\delta\Lambda^T\mathbf{f}_{int,\epsilon}^{(I)} \qquad (3.71)$$

where

$$\mathbf{M}^{(I)} = \int_\Omega \mathbf{H}_u^T\mathbf{R}\mathbf{H}_u d\Omega \qquad (3.72)$$

$$\mathbf{K}_{uu}^{(I)} = \int_\Omega \mathbf{B}_u^T(1-\omega^{(I)})\mathbf{D}^e\mathbf{B}_u d\Omega \qquad (3.73)$$

$$\mathbf{K}_{u\epsilon}^{(I)} = -\int_{\Omega} \mathbf{B}_u^T \mathbf{D}^e \boldsymbol{\epsilon}^{(I)} \left(\frac{\partial \omega}{\partial \kappa}\right)^{(I)} \left(\frac{\partial \kappa}{\partial \bar{\epsilon}_{eq}}\right)^{(I)} \mathbf{H}_\epsilon d\Omega \tag{3.74}$$

$$\mathbf{K}_{\epsilon\epsilon}^{(I)} = \int_{\Omega} (\mathbf{H}_\epsilon^T \mathbf{H}_\epsilon + \mathbf{B}_\epsilon^T c \mathbf{B}_\epsilon) d\Omega \tag{3.75}$$

$$\mathbf{K}_{\epsilon u}^{(I)} = -\int_{\Omega} \mathbf{H}_\epsilon^T \left[\left(\frac{\partial \epsilon_{eq}}{\partial \epsilon}\right)^{(I)}\right]^T \mathbf{B}_u d\Omega \tag{3.76}$$

$$\mathbf{f}_{ext,u}^{(I+1)} = \int_{\Omega} \mathbf{H}_u^T \mathbf{p}^{(I+1)} d\Omega + \int_{\partial\Omega_t} \mathbf{H}_u^T \mathbf{t}^{(I+1)} d\Gamma \tag{3.77}$$

$$\mathbf{f}_{int,u}^{(I)} = \int_{\Omega} \mathbf{B}_u^T \boldsymbol{\sigma}^{(I)} d\Omega \tag{3.78}$$

$$\mathbf{f}_{int,\epsilon}^{(I)} = \int_{\Omega} \left(\mathbf{H}_\epsilon^T \Lambda^{(I)} + \mathbf{B}_\epsilon^T c \mathbf{B}_\epsilon \Lambda^{(I)} - \mathbf{H}_\epsilon^T \epsilon_{eq}^{(I)}\right) d\Omega \tag{3.79}$$

Since equations 3.70 and 3.71 must hold for any arbitrary $\delta\mathbf{a}$ and $\delta\Lambda$ the semi-discretized weak forms of field equations then give

$$\mathbf{M}^{(I)} \ddot{\mathbf{a}}^{(I+1)} + \mathbf{K}_{uu}^{(I)} d\mathbf{a}^{(I)} + \mathbf{K}_{u\epsilon}^{(I)} d\Lambda^{(I)} = \mathbf{f}_{ext,u}^{(I+1)} - \mathbf{f}_{int,u}^{(I)} \tag{3.80}$$

$$\mathbf{K}_{\epsilon u}^{(I)} d\mathbf{a}^{(I)} + \mathbf{K}_{\epsilon\epsilon}^{(I)} d\Lambda^{(I)} = -\mathbf{f}_{int,\epsilon}^{(I)} \tag{3.81}$$

We apply the implicit time integration scheme of Newmark family to Eqs. 3.80 and 3.81 to obtain fully discretized system of equations for the initial value problem. Following the procedure described in section 2.4, we obtain

$$\begin{bmatrix} \mathbf{K}_{uu}^{(I)} + c_0 \mathbf{M}^{(I)} & \mathbf{K}_{u\epsilon}^{(I)} \\ \mathbf{K}_{\epsilon u}^{(I)} & \mathbf{K}_{\epsilon\epsilon}^{(I)} \end{bmatrix} \begin{bmatrix} d\mathbf{a}^{(I)} \\ d\Lambda^{(I)} \end{bmatrix} = \begin{bmatrix} \mathbf{f}_{ext,u}^{(I+1)} - \mathbf{f}_{int,u}^{(I)} - \mathbf{M}^{(I)} \ddot{\mathbf{a}}^{(I)} \\ -\mathbf{f}_{int,\epsilon}^{(I)} \end{bmatrix} \tag{3.82}$$

which can be solved by using a full Newton-Raphson procedure. The algorithmic treatment for the global iteration process is similar as the one outlined in Table 2.1 in section 2.4. While the procedure to update the stress and strain relation is outlined in Table 3.3.

## 3.2.2 Strain-based transient-gradient damage model

Enhanced continuum models perform worse at the later stages of failure because they can not reflect the development of discrete surfaces. Where a discrete surface should develop the strain and strain rate approach infinity, which can lead to spurious spreading of inelastic deformations, damage growth and for rate dependent models even a hardening effect since strain rate becomes very high (cf. [6, 16]).

In order to represent the complete failure process, displacement discontinuities can be incorporated at certain stages or remeshing techniques should be used. For the implicit gradient damage model described in the previous section, Geers ([6]) proposed to adopt a variable length scale, and eliminate the interaction between crack and the surrounding material.

The governing system of partial differential equations now read (cf. Eq. 2.1 and Eq. 3.47)

$$\mathbf{L}^T \boldsymbol{\sigma} + \mathbf{p} = \mathbf{R}\ddot{\mathbf{u}} \qquad\qquad in \ \Omega \tag{3.83}$$

$$\bar{\epsilon}_{eq}(\mathbf{x}) - \zeta \nabla^2 \bar{\epsilon}_{eq}(\mathbf{x}) = \epsilon_{eq}(\mathbf{x}) \qquad\qquad in \ \Omega \tag{3.84}$$

Instead of a constant gradient parameter as in Eq. 3.47, a variable $\zeta$ is used which is denoted as *gradient activity*. It models the mobilized nonlocal coupling between particles at microlevel.

16

---

1. update strain increment, total strain and nonlocal equivalent strain at integration point

   $$\Delta \epsilon , \qquad \epsilon , \qquad \bar{\epsilon}_{eq}$$

2. compute equivalent strain $\epsilon_{eq}(\epsilon)$, $\frac{\partial \epsilon_{eq}}{\partial \epsilon}$

3. evaluate the loading function $f = \bar{\epsilon}_{eq} - \kappa_0$

   where $\kappa_0$ is the converged value of $\kappa$ at the end of the previous load increment

4. if loading($f \geq 0$) then $\kappa = \bar{\epsilon}_{eq}$

   else $\quad \kappa = \kappa_0$

5. compute damage variable and its derivative with respect to $\kappa$: $\quad \omega = \omega(\kappa)$, $\frac{\partial \omega}{\partial \kappa}$

6. compute the new stress $\sigma = (1 - \omega)\mathbf{D}^e \epsilon$

---

Table 3.3: Updating the stress and strain for implicit gradient damage model

For the strain-based transient-gradient damage model, we use the following gradient activity evolution law

$$\zeta = \begin{cases} c \left( \frac{\epsilon_{eq}}{\epsilon_{eq,\zeta}} \right)^{n_\zeta} & \text{if } \epsilon_{eq} \leq \epsilon_{eq,\zeta} \\ c & \text{if } \epsilon_{eq} > \epsilon_{eq,\zeta} \end{cases} \tag{3.85}$$

where $c$ and $n_\zeta$ are two constants. This evolution law implies that nonlocal coupling is mobilized more and more as the local deformation increases, while it gradually vanishes in the unloaded material surrounding cracks. Thus the large strain in cracks gives little effect to surrounding material, and the spurious damage growth at the crack faces is prevented.

A three-field formulation is used to achieve stability, $[\mathbf{u}, \bar{\epsilon}_{eq}, \varsigma]$. The weak forms of the governing equations are written as (cf. Eq. 2.11 and Eq. 3.58)

$$\int_\Omega \delta \mathbf{u}^T [\mathbf{L}^T \sigma + \mathbf{p} - \mathbf{R}\ddot{\mathbf{u}}] d\Omega = 0 \tag{3.86}$$

$$\int_\Omega \delta \bar{\epsilon}_{eq} (\bar{\epsilon}_{eq} - \varsigma \nabla^2 \bar{\epsilon}_{eq}) d\Omega = \int_\Omega \delta \bar{\epsilon}_{eq} \epsilon_{eq} d\Omega \tag{3.87}$$

$$\int_\Omega \delta \varsigma (\varsigma - \zeta) d\Omega = 0 \tag{3.88}$$

For implementation using the finite element method, the continuous fields $\mathbf{u}(\mathbf{x},t)$, $\bar{\epsilon}_{eq}(\mathbf{x},t)$ and $\varsigma(\mathbf{x},t)$ are discretized by using shape functions.

$$\mathbf{u}(\mathbf{x}, t) = \mathbf{H}_u(\mathbf{x})\mathbf{a}(t) \tag{3.89}$$

$$\ddot{\mathbf{u}}(\mathbf{x}, t) = \mathbf{H}_u(\mathbf{x})\ddot{\mathbf{a}}(t) \tag{3.90}$$

$$\dot{\epsilon}(\mathbf{x}, t) = \mathbf{B}_u(\mathbf{x})\dot{\mathbf{a}}(t) = \mathbf{L}\mathbf{H}_u\dot{\mathbf{a}}(t) \tag{3.91}$$

$$\bar{\epsilon}_{eq}(\mathbf{x}, t) = \mathbf{H}_\epsilon(\mathbf{x})\Lambda(t) \tag{3.92}$$

$$\nabla\bar{\epsilon}_{eq}(\mathbf{x}, t) = \mathbf{B}_\epsilon\Lambda(t) = \nabla\mathbf{H}_\epsilon(\mathbf{x})\Lambda(t) \tag{3.93}$$

$$\varsigma(\mathbf{x}, t) = \mathbf{H}_\varsigma(\mathbf{x})\Upsilon(t) \tag{3.94}$$

$$\nabla\varsigma(\mathbf{x}, t) = \mathbf{B}_\varsigma\Upsilon(t) = \nabla\mathbf{H}_\varsigma(\mathbf{x})\Upsilon(t) \tag{3.95}$$

With the aid of Green's formula of integration by parts, we obtain

$$\int_\Omega \delta\mathbf{u}^T[\mathbf{R}\ddot{\mathbf{u}}]d\Omega + \int_\Omega \delta\epsilon^T\sigma d\Omega = \int_\Omega \delta\mathbf{u}^T\mathbf{p}d\Omega + \int_{\partial\Omega_t} \delta\mathbf{u}^T\mathbf{t}d\Gamma \tag{3.96}$$

$$\int_\Omega \left[\delta\bar{\epsilon}_{eq}\bar{\epsilon}_{eq} + \nabla\delta\bar{\epsilon}_{eq}^T\varsigma\nabla\bar{\epsilon}_{eq} + \delta\bar{\epsilon}_{eq}\nabla\varsigma^T\nabla\bar{\epsilon}_{eq}\right]d\Omega = \int_\Omega \delta\bar{\epsilon}_{eq}\epsilon_{eq}d\Omega \tag{3.97}$$

$$\int_\Omega \delta\varsigma\left[\varsigma - \zeta\right]d\Omega = 0 \tag{3.98}$$

where boundary condition $\mathbf{N}^T\sigma = \mathbf{t}$ (i.e. Eq. 2.5) and additional boundary condition $\varsigma\nabla\bar{\epsilon}_{eq}{}^T\mathbf{n} = 0$ (cf. Eq. 3.48) are used.

A linearization process and time integration scheme similar to that described in section 3.2.1 are used. Then a full discrete system of governing equations is obtained (cf. 3.82)

$$\begin{bmatrix} \mathbf{K}_{uu}^{(I)} + c_0\mathbf{M}^{(I)} & \mathbf{K}_{u\epsilon}^{(I)} & 0 \\ \mathbf{K}_{\epsilon u}^{(I)} & \mathbf{K}_{\epsilon\epsilon}^{(I)} & \mathbf{K}_{\epsilon\varsigma}^{(I)} \\ \mathbf{K}_{\varsigma u}^{(I)} & 0 & \mathbf{K}_{\varsigma\varsigma}^{(I)} \end{bmatrix} \begin{bmatrix} d\mathbf{a}^{(I)} \\ d\Lambda^{(I)} \\ d\Upsilon^{(I)} \end{bmatrix} = \begin{bmatrix} \mathbf{f}_{ext,u}^{(I+1)} - \mathbf{f}_{int,u}^{(I)} - \mathbf{M}^{(I)}\ddot{\mathbf{a}}^{(I)} \\ -\mathbf{f}_{int,\epsilon}^{(I)} \\ -\mathbf{f}_{int,\varsigma}^{(I)} \end{bmatrix} \tag{3.99}$$

where subscripts t+$\Delta$t are omitted for simplicity. The expressions of the sub-matrices and the vectors are listed below

$$\mathbf{M}^{(I)} = \int_\Omega \mathbf{H}_u^T\mathbf{R}\mathbf{H}_u d\Omega \tag{3.100}$$

$$\mathbf{K}_{uu}^{(I)} = \int_\Omega \mathbf{B}_u^T(1 - \omega^{(I)})\mathbf{D}^e\mathbf{B}_u d\Omega \tag{3.101}$$

$$\mathbf{K}_{u\epsilon}^{(I)} = -\int_\Omega \mathbf{B}_u^T\mathbf{D}^e\epsilon^{(I)}\left(\frac{\partial\omega}{\partial\kappa}\right)^{(I)}\left(\frac{\partial\kappa}{\partial\bar{\epsilon}_{eq}}\right)^{(I)}\mathbf{H}_\epsilon d\Omega \tag{3.102}$$

$$\mathbf{K}_{\epsilon u}^{(I)} = -\int_\Omega \mathbf{H}_\epsilon^T\left[\left(\frac{\partial\epsilon_{eq}}{\partial\epsilon}\right)^{(I)}\right]^T\mathbf{B}_u d\Omega \tag{3.103}$$

$$\mathbf{K}_{\epsilon\epsilon}^{(I)} = \int_\Omega \left[\mathbf{H}_\epsilon^T\mathbf{H}_\epsilon + \mathbf{B}_\epsilon^T\mathbf{H}_\varsigma\Upsilon^{(I)}\mathbf{B}_\epsilon + \mathbf{H}_\epsilon^T\left[\Upsilon^{(I)}\right]^T\mathbf{B}_\varsigma^T\mathbf{B}_\epsilon\right]d\Omega \tag{3.104}$$

$$\mathbf{K}_{\epsilon\varsigma}^{(I)} = \int_\Omega \left[\mathbf{B}_\epsilon^T\mathbf{B}_\epsilon\Lambda^{(I)}\mathbf{H}_\varsigma + \mathbf{H}_\epsilon^T\left[\Lambda^{(I)}\right]^T\mathbf{B}_\epsilon^T\mathbf{B}_\varsigma\right]d\Omega \tag{3.105}$$

$$\mathbf{K}_{\varsigma u}^{(I)} = -\int_\Omega \mathbf{H}_\varsigma^T\left(\frac{\partial\varsigma}{\partial\epsilon_{eq}}\right)^{(I)}\left[\left(\frac{\partial\epsilon_{eq}}{\partial\epsilon}\right)^{(I)}\right]^T\mathbf{B}_u d\Omega \tag{3.106}$$

$$\mathbf{K}_{\varsigma\varsigma}^{(I)} = -\int_\Omega \mathbf{H}_\varsigma^T\mathbf{H}_\varsigma d\Omega \tag{3.107}$$

$$\mathbf{f}_{ext,u}^{(I+1)} = \int_\Omega \mathbf{H}_u^T\mathbf{p}^{(I+1)}d\Omega + \int_{\partial\Omega_t} \mathbf{H}_u^T\mathbf{t}^{(I+1)}d\Gamma \tag{3.108}$$

$$\mathbf{f}_{int,u}^{(I)} = \int_\Omega \mathbf{B}_u^T\sigma^{(I)}d\Omega \tag{3.109}$$

$$\mathbf{f}_{int,\epsilon}^{(I)} = \int_\Omega \mathbf{H}_\epsilon^T\mathbf{H}_\epsilon\Lambda^{(I)} + \mathbf{B}_\epsilon^T\mathbf{H}_\varsigma\Upsilon^{(I)}\mathbf{B}_\epsilon\Lambda^{(I)} + \mathbf{H}_\epsilon^T\left[\Upsilon^{(I)}\right]^T\mathbf{B}_\varsigma^T\mathbf{B}_\epsilon\Lambda^{(I)}d\Omega - \int_\Omega \mathbf{H}_\epsilon^T\epsilon_{eq}^{(I)}d\Omega \tag{3.110}$$

$$\mathbf{f}_{int,\varsigma}^{(I)} = -\int_\Omega \mathbf{H}_\varsigma^T\zeta^{(I)}d\Omega + \int_\Omega \mathbf{H}_\varsigma^T\mathbf{H}_\varsigma\Upsilon^{(I)}d\Omega \tag{3.111}$$

The procedure for updating stress and strain at integration point level is the same as in Table 3.3, while the global incremental-iterative procedure is similar to that outlined in Table 2.1.

# Chapter 4

# One-dimensional localization problem

In this chapter, we treat a one-dimensional bar problem under impact tensile loading. The continuum models introduced in Chapter 3 are used. The main purpose is to demonstrate the numerical consequence of the ill-posedness of the initial value problem for standard plastic model and local damage model, and the regularization effect of rate dependent viscoplasticity models and gradient enchanced damage models. Only the mode-I localization problem is considered. The results can be extended to the mode-II problem if an appropriate yield function is used. The one-dimensional bar used in the numerical simulation is sketched in Fig. 4.1. The consistent mass matrix is adopted in the simulation.
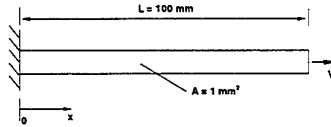


Figure 4.1: The one-dimensional bar problem.

## 4.1 Standard elastoplastic model

The standard plastic model described in section 3.1.1 is tested first. A rankine yield criterion, an associative flow rule, a linear softening law and a strain hardening/softening hypothesis are utilized. The material parameters are listed in Table 4.1. Use has been made of a two-noded line element. The bar is divided into 10, 20, 40 and 80 elements, respectively. A constant tensile impact velocity V = 450 mm/s is applied on the loading end of the bar, the bar responses linear elastically until the loading wave reaches the left boundary. The doubling in stress due to reflection of tensile wave causes the initiation of yielding. The material enters the softening regime and strain localization zone emerges. A time step $\Delta t = 0.5$ $\mu$s is used for all calculations.

Table 4.1: Material parameters for standard elastoplastic model in the one-dimensional problem.

| $E$ | $E_n$ | $\bar{\sigma}_0$ | $\rho$ |
|---|---|---|---|
| 3.5e+4 $MPa$ | -3.5e+3 $MPa$ | 5.0 $MPa$ | 2.0e-9 $Ns^2/mm^4$ |

The strain and stress profiles for different meshes at time t = 36.0 $\mu$s $\approx \frac{3}{2}\frac{L}{c_e}$ ($c^e$ is elastic wave velocity) are shown in Fig. 4.2. It can be seen that strain localization occurs in one element (one integration point) which is the smallest possible zone. Hence the width of the localization zone decreases upon mesh refinement. The amount of wave reflection depends on the discretization. As soon as the stress has become zero, the localization zone (i.e. one integration point near the left boundary) acts as a free boundary on which tensile wave reflects as a pressure wave (cf. [11]). Note that all results for the one-dimensional problem are the values of variables at individual integration points.
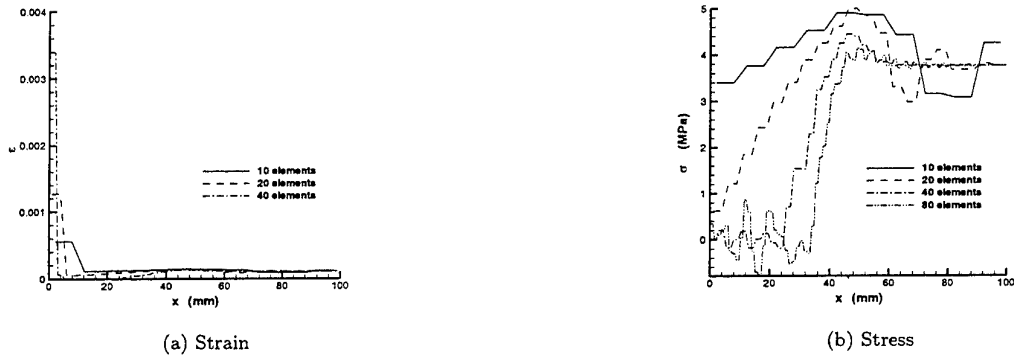
19

(a) Strain



(b) Stress

Figure 4.2: The strain profiles (a) and stress profiles (b) for different meshes.

## 4.2 Perzyna viscoplastic model

The Rankine yield criterion combined with Perzyna viscoplasticity, an associative flow rule, a linear softening law and a strain hardening/softening hypothesis are used. The material parameters are given in Table 4.2. Use has been made of a two-noded line element. A constant impact tensile velocity V = 450 mm/s is applied on the loading end.

Table 4.2: Material parameters for Perzyna viscoplastic model in one-dimensional problem.

| $E$ | $E_n$ | $\bar{\sigma}_0$ | $\eta$ | $N$ | $\rho$ |
|---|---|---|---|---|---|
| 3.5e+4 $MPa$ | -3.5e+3 $MPa$ | 5.0 $MPa$ | 200.0 $s^{-1}$ | 1.0 | 2.0e-9 $Ns^2/mm^4$ |



(a) Strain



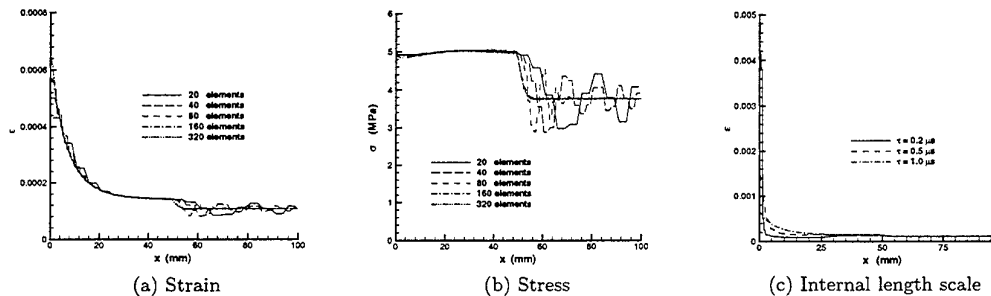(b) Stress



(c) Internal length scale
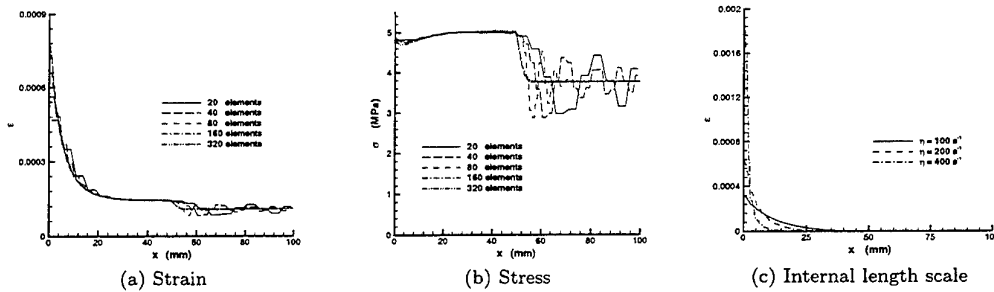
Figure 4.3: The strain profiles for different meshes (a), the stress profiles for different meshes (b) and the strain profiles for different internal length scales (c).

The strain and stress profiles for different discretizations (20, 40, 80, 160 and 320 elements) at time t = 36.0 $\mu$s are shown in Figs. 4.3a and b. Constant time steps $\Delta t$ = 0.10 $\mu$s for the calculation with 320 elements and $\Delta t$ = 0.15 $\mu$s for other calculations are used. The results show an exponential decrease of strain after the reflection on the fixed end. For the coarse meshes of 20, 40 and 80 elements, the results are not identical. However, a unique solution is obtained when the mesh is refined to 160 and 320 elements. The localization zone converges to a finite, constant band width upon mesh refinement. The mesh independent partial reflection on the localization zone can be seen from the stress profiles in Fig. 4.3b. This result shows that the viscous effect has a regularization effect.

The influence of viscosity parameter $\eta$ on the width of localization zone can be seen in Fig. 4.3c for the mesh with 160 elements. The width of localization zone increases with the decrease of viscosity parameter, i.e. the increase of viscous effect.

## 4.3 Duvaut-Lions viscoplastic model

The Rankine yield criterion combined with Duvaut-Lions viscoplasticity, an associative flow rule, a linear softening law and a strain hardening/softening hypothesis are used. The material parameters are given in Table 4.3. Use has been made of a two-noded line element. A constant impact tensile velocity V = 450 mm/s is applied on the loading end.

Table 4.3: Material parameters for Duvaut-Lions viscoplastic model in one-dimensional problem.

| $E$ | $E_n$ | $\bar{\sigma}_0$ | $\tau$ | $\rho$ |
|---|---|---|---|---|
| 3.5e+4 $MPa$ | -3.5e+3 $MPa$ | 5.0 $MPa$ | 1.0 $\mu s$ | 2.0e-9 $Ns^2/mm^4$ |



(a) Strain          (b) Stress          (c) Internal length scale

Figure 4.4: The strain profiles for different meshes (a), the stress profiles for different meshes (b) and the strain profiles for different internal length scales (c).

The strain and stress profiles for different discretizations (20, 40, 80, 160 and 320 elements) at time t = 36.0 $\mu s$ are shown in Figs. 4.4a and b. Constant time steps $\Delta t$ = 0.10 $\mu s$ for the calculation with 320 elements and $\Delta t$ = 0.15 $\mu s$ for other calculations are used. The convergence to a unique solution upon mesh refinement for the strain localization and wave reflection show that physically realistic results can be obtained. The influence of the relaxation time $\tau$ on the width of the localization zone is presented in Fig. 4.4c.

For the one-dimensional case, a dispersion analysis can be carried out for the Perzyna and the Duvaut-Lions viscoplastic model (cf. [11]). The obtained internal length scale for the Perzyna model is $l = \frac{2\bar{\sigma}_0 C_e}{\eta E}$ for mode-I localization. A similar expression for the Duvaut-Lions model is $l = 2\tau C_e$. When the internal length scales l for the two models are equal, almost identical numerical results can be obtained.

## 4.4 Local damage model

A local damage model combined with a linear softening damage evolution law and an equivalent strain $\epsilon_{eq} = \epsilon$ is adopted in this section. The material parameters are presented in Table 4.4 . Use has been made of a two-noded line element. The bar is divided into 10, 20, 40, 80 elements. A constant impact tensile velocity V = 450 mm/s is applied on the loading end. A time step $\Delta t$ = 0.5 $\mu s$ is used for all calculations.

Table 4.4: Material parameters for local damage model in one-dimensional problem.

| $E$ | $\kappa_i$ | $\kappa_c$ | $\rho$ |
|---|---|---|---|
| 3.5e+4 $MPa$ | 1.43e-4 | 1.43e-3 | 2.0e-9 $Ns^2/mm^4$ |

The strain, stress and damage profiles at time t = 36.0 $\mu s$ for different meshes are shown in Fig. 4.5. Strain localization occurs in one element which is the smallest possible zone. The width of the strain localization zone and the amplitude of strain and damage exhibit mesh dependence (cf. [2] ). The results are similar to that of a standard elastoplastic model in section 4.1.
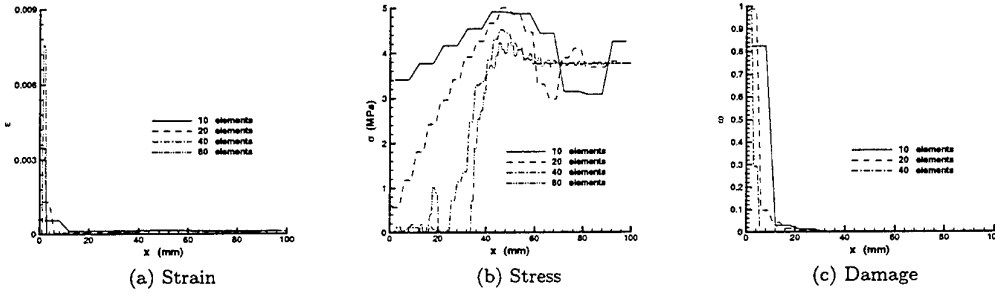
(a) Strain   (b) Stress   (c) Damage

Figure 4.5: The strain profiles (a), stress profiles (b) and damage profiles (c) for different meshes.

## 4.5 Constant gradient damage model

The second-order implicit constant gradient damage model, described in section 3.2.1, is used to illustrate the reguralizing effect of the gradient enhancement. The linear softening damage evolution law and the equivalent strain $\epsilon_{eq} = \epsilon$ are applied in this model. Use has been made of a three-noded line element with quadratic interpolation for the displacement and linear interpolation for the nonlocal equivalent strain $\bar{\epsilon}_{eq}$. A two-point Gauss quadrature scheme is used. The material parameters are listed in Table 4.5. A constant impact tensile velocity $V = 450$ mm/s is applied on the loading end.

Table 4.5: Material parameters for constant gradient damage model in one-dimensional problem.

| $E$ | $\kappa_i$ | $\kappa_c$ | $c$ | $\rho$ |
|---|---|---|---|---|
| 3.5e+4 $MPa$ | 1.43e-4 | 1.43e-3 | 3.0 $mm^2$ | 2.0e-9 $Ns^2/mm^4$ |



(a) Strain   (b) Stress   (c) Damage
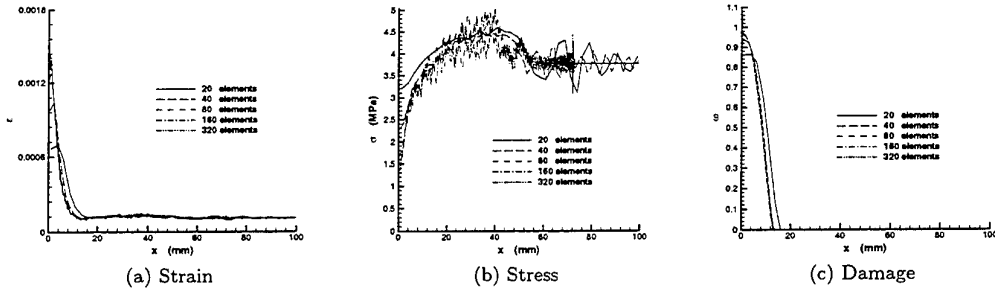
Figure 4.6: The strain profiles (a), stress profiles (b) and damage profiles (c) for different meshes.

The numerical results are presented in Fig. 4.6 including the strain, stress and damage profiles for different discretizations (20, 40, 80, 160 and 320 elements) at time $t = 36.0$ $\mu s$. Constant time steps $\Delta t = 0.10$ $\mu s$ for the calculation with 320 elements and $\Delta t = 0.15$ $\mu s$ for other calculations are used. Upon mesh refinement, the numerical solution shows convergence towards a unique solution. Whereas the 20 element mesh is still too coarse, the 40 element mesh already gives a reasonable prediction of the width of the localization zone. Hence the implicit gradient enhanced damage model can carry out failure analysis in an objective manner. However, the mesh must be fine enough in order to capture the intense straining in the localization zone. This holds true for a higher-order spatial derivatives enhanced continuum model as well as for a higher-order temporal derivatives enhanced continuum model. The influence of gradient parameter c on the width of localization zone is presented in Fig. 4.7. The width of localization zone increases with the increase of the parameter c. In the calculations shown in this figure, the mesh of 160 elements is used. The stress oscillation is due to artificial higher-order frequencies introduced by semi-discretization of the equation of motion. Algorithmic damping can be used to exclude these high-frequent responses. However, by introducing numerical damping in the Newmark scheme the accuracy deteriorates.
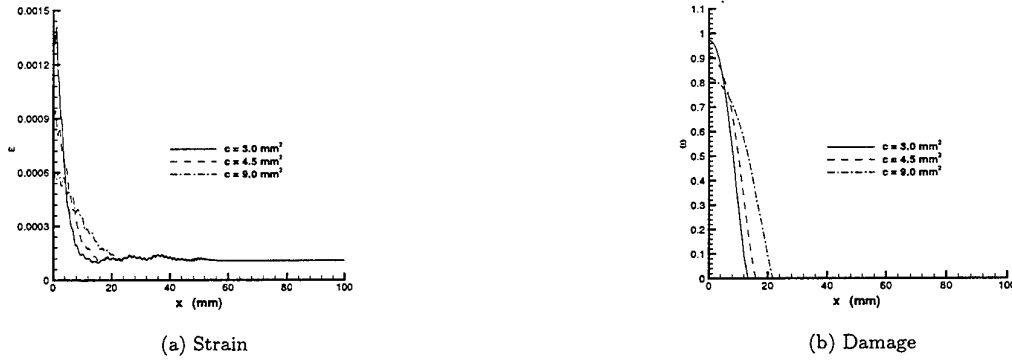
(a) Strain

(b) Damage

Figure 4.7: The strain profiles (a) and damage profiles (b) for different gradient parameter c.

## 4.6 Strain-based transient-gradient damage model

Because of the deficiency of the constant gradient enhanced damage model at final stages of failure a variable gradient enchanced damage model has been introduced in section 3.2.2. In this section, the one-dimensional dynamic tensile bar problem is used to compare these two models numerically. Instead of the linear softening law, an exponential softening law is used. The equivalent strain is defined as $\epsilon_{eq}$ = $\epsilon$. The material parameters for both models are listed in Table 4.6 and 4.7, respectively. Use has been made of a three-noded line element, where quadratic interpolation for the displacement field, linear interpolation for the nonlocal equivalent strain field and linear interpolation for the gradient activity field $\varsigma$ are utilized. The bar is divided into 160 elements with $\Delta t = 0.15$ $\mu s$ for the constant gradient damage model and 640 elements with $\Delta t = 0.0375$ $\mu s$ for a strain-based transient-gradient damage model. A constant impact tensile velocity V = 590 mm/s is applied on the loading end of the bar.

Table 4.6: Material parameters for constant gradient damage model.

| $E$ | $\kappa_i$ | $\alpha$ | $\beta$ | $c$ | $\rho$ |
|---|---|---|---|---|---|
| 3.5e+4 $MPa$ | 1.43e-4 | 0.96 | 2400.0 | 3.0 $mm^2$ | 2.0e-9 $Ns^2/mm^4$ |

Table 4.7: Material parameters for strain-based transient-gradient damage model.

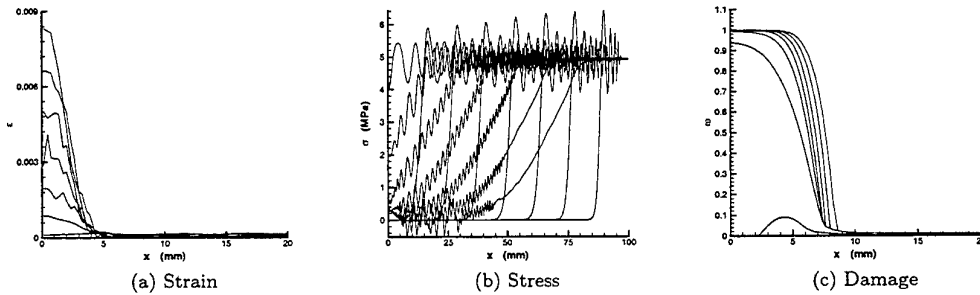| $E$ | $\kappa_i$ | $\alpha$ | $\beta$ | $c$ | $\epsilon_{eq,\varsigma}$ | $n_\varsigma$ | $\rho$ |
|---|---|---|---|---|---|---|---|
| 3.5e+4 $MPa$ | 1.43e-4 | 0.96 | 2400.0 | 9.0 $mm^2$ | 1.43e-3 | 1.1 | 2.0e-9 $Ns^2/mm^4$ |



(a) Strain

(b) Stress

(c) Damage

Figure 4.8: Stroboscopic development of strain (a), stress(b) and damage (c) for constant gradient damage model.

The numerical result for a constant gradient damage model predicts a physically unacceptable growth of the damage zone when the damage in the localization zone approaches the critical value (i.e. $\omega \rightarrow 1$).

24



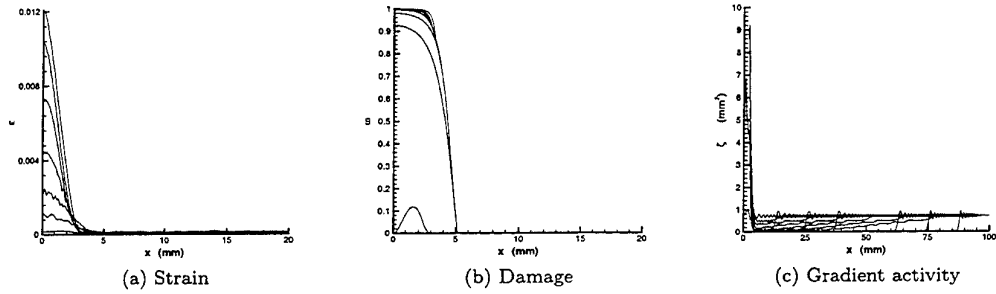| (a) Strain | (b) Damage | (c) Gradient activity |

Figure 4.9: Stroboscopic development of strain (a), damage (d) and gradient activity (c).

This is presented in Fig. 4.8. The reason is that the intense increase of local strain in the localization zone results in an increase of the local equivalent strain. The diffusion equation maps this increase onto the nonlocal equivalent strain, which provokes an increase of damage. The weakening of the damaged zone results again in larger strains. The calculation is conducted until t = 42.0 $\mu$s and the interval between the plots is 3.0 $\mu$s. The damage plateau of the small amplitude in the other part of the bar is due to the stress oscillation of the loading wave. It can be avoided when the time step is reduced to $\Delta t = 0.10$ $\mu$s.

The stroboscopic development of strain and damage for the strain-based transient-gradient damage model are given in Figs. 4.9a and b. It can be seen that this model can preserve the width of localization zone and avoid the spurious spreading of damage. The development of gradient activity is presented in Fig. 4.9c. Due to the steep change in gradient activity, the mesh must be finer than that used for a constant gradient damage model.

# Chapter 5

# Two-dimensional microstructure analysis

In this chapter, a few square block microstructures with a width of 13.774mm are used as the representative volume element for concrete to investigate the dynamic response of concrete at meso-level. The continuum models described in chapter 3 are used. The structures and the finite element discretization are shown in Fig. 5.1. Three microstructures are used with two meshes for stucture one. The microstructures are composed of aggregates, matrix and an interfacial transition zone (ITZ). Hence, three sets of material parameters are used. A three-noded triangular element is used for the discretization and a lumped mass matrix is adopted for the numerical simulation. The plane stress condition is assumed. A constant time step $\Delta t = 0.01$ $\mu$s is chosen for all the calculations. The boundary and loading conditions are illustrated in Fig. 5.2, the bottom of the microstructure is fixed while at the top edge a constant impact tensile velocity is applied.
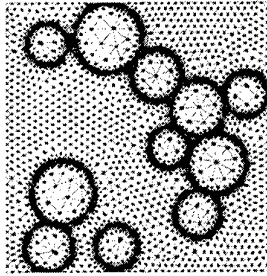


(a) Structure one: mesh 1A; 4487 nodes, 8788 elements
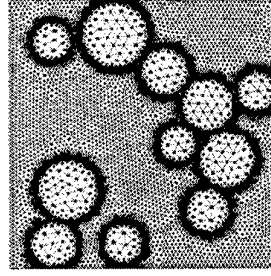
(b) Structure one: mesh 1B; 7317 nodes, 14327 elements
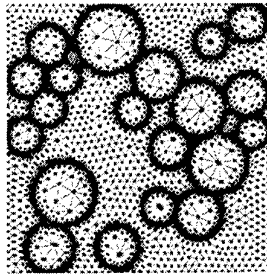
(c) Structure two: 5815 nodes, 11423 elements
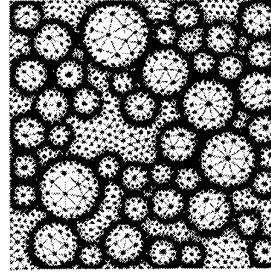
(d) Structure three: 7951 nodes, 15640 elements

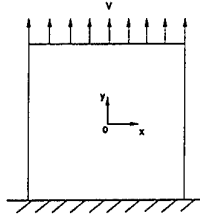Figure 5.1: Microstructure and finite element discretization.

Figure 5.2: Boundary and loading conditions for the microstructures.

## 5.1 Standard elastoplastic model

The material parameters are shown in Table 5.1 for the standard elastoplastic model described in section 3.1.1. A Von Mises yield criterion, an associative flow rule, an exponential softening law and a strain hardening/softening hypothesis are utilized in the material model.

Table 5.1: Material parameters for standard elastoplastic model

| Matrix | | Aggregate | | ITZ | |
|---|---|---|---|---|---|
| $E$ | 3.5e+4 $MPa$ | $E$ | 5.5e+4 $MPa$ | $E$ | 3.5e+4 $MPa$ |
| $\nu$ | 0.3 | $\nu$ | 0.3 | $\nu$ | 0.3 |
| $\bar{\sigma}_0$ | 5.25 $MPa$ | $\bar{\sigma}_0$ | 41.25 $MPa$ | $\bar{\sigma}_0$ | 3.5 $MPa$ |
| $\bar{\sigma}_\infty$ | 5.25e-2 $MPa$ | $\bar{\sigma}_\infty$ | 41.25e-2 $MPa$ | $\bar{\sigma}_\infty$ | 3.5e-2 $MPa$ |
| $\beta$ | 200.0 | $\beta$ | 200.0 | $\beta$ | 200.0 |
| $\rho$ | 2.0e-9 $Ns^2/mm^4$ | $\rho$ | 2.0e-9 $Ns^2/mm^4$ | $\rho$ | 2.0e-9 $Ns^2/mm^4$ |

A constant impact tensile velocity V = 300 mm/s is applied at the loading edge of microstructure one. The development of the plastic strain measure $\kappa$ for mesh 1A (cf. Fig. 5.1a) is shown in Fig. 5.3. We observe that before the loading waves arrive at the fixed edge (see Fig. 5.3a), the material in some ITZs has already failed. Plastic straining is localized in the ITZs. After the loading waves are reflected at the fixed bottom edge the localization zones in the ITZs begin to propagate into the matrix. At time t = 8.0 $\mu$s, the waves which were reflected from the fixed edge have reflected on the loading edge. Due to this further loading, the localization zones, initiated from the ITZs, propagate through the matrix and connect with each other, while the plastic strain level is comparable with that in the ITZs. No localization zones can be seen initiating from the matrix material. The aggregates can not fail during the this process.



(a) t = 2.0 $\mu$s



(b) t = 8.0 $\mu$s
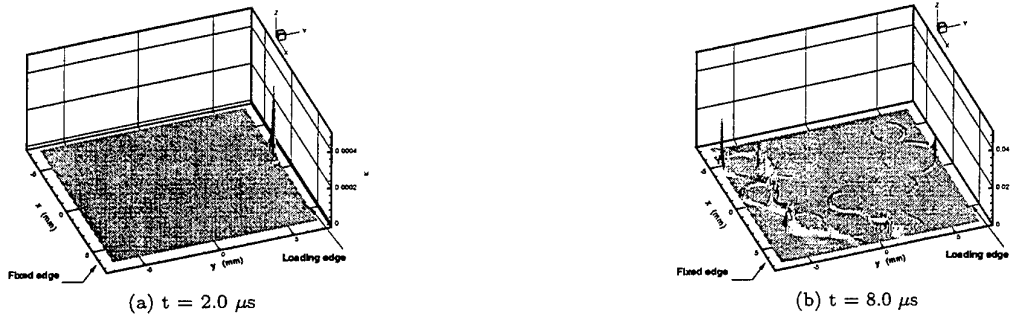
Figure 5.3: The development of history parameter $\kappa$.

The width of the localization zone is about the size of one elment. This is exhibited by the deformation pattern plot in Fig. 5.4a, which is amplified with a factor of 1200. When a finer discretization mesh 1B is used, the localization zones are still concentrated in one row of elements, see Fig. 5.4b. This is the
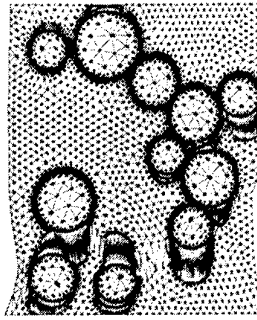
(a) mesh 1A, t = 8.0 $\mu$s
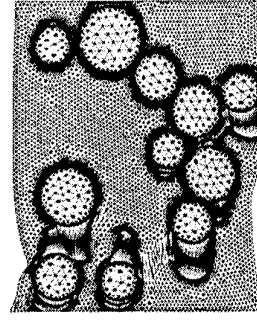
(b) mesh 1B, t = 8.0 $\mu$s

Figure 5.4: The deformation patterns for two discretizations at time t = 8.0 $\mu$s.
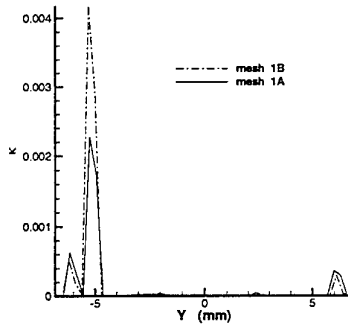


(a) Central vertical cross section plot
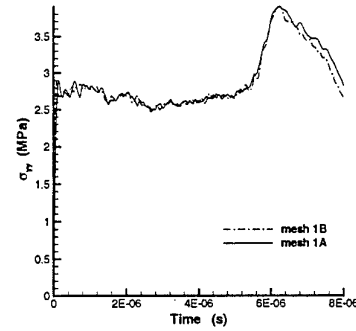
(b) Reaction stress history

Figure 5.5: The profiles of parameter $\kappa$ along the central vertical cross section at time t = 8.0 $\mu$s (a) and the average reaction stress component $\sigma_{yy}$ versus time (b).
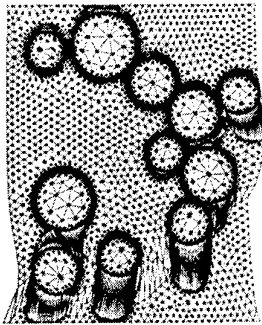


(a) mesh 1A, t = 8.0 $\mu$s
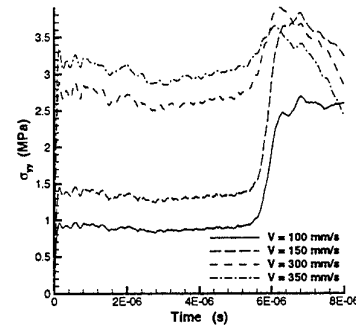
(b) Reaction stress history

Figure 5.6: The deformation pattern with an impact velocity V = 350 mm/s (a) and the profiles for the average reaction stress component $\sigma_{yy}$ versus time with different impact velocities.

numerical consequence of the ill-posedness of the initial value problem when a classical continuum model combined with a softening material law is utilized. The mesh dependence of the solution is also shown in Fig. 5.5, where the profiles of $\kappa$ along the central vertical cross section of the microstructure at t = 8.0 $\mu$s for different meshes are plotted (left) and the average reaction stress component $\sigma_{yy}$ along the loading

edge versus time is shown (right).

Fig. 5.6 presents the numerical results for different impact velocities. The peak value of the average reaction stress increases with the increase of the impact velocity when the impact velocity is relatively low. When the impact velocity is further increased, a more intense plastic straining appears in the matrix and ITZs and a negative loading rate dependence is obtained.
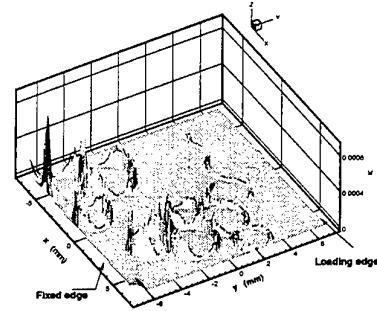
## 5.2 Perzyna viscoplastic model

For the Perzyna viscoplastic model, a Von Mises yield criterion, an associative plastic flow rule, an exponential softening law and a strain hardening/softening hypothesis are applied. The material parameters are listed in Table 5.2.

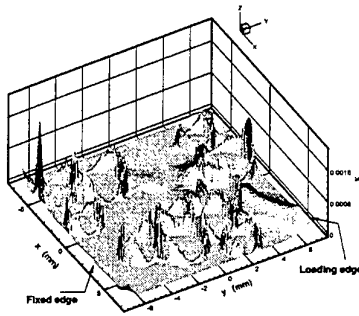Table 5.2: Material parameters for Perzyna viscoplastic model

| Matrix | | Aggregate | | ITZ | |
|---|---|---|---|---|---|
| $E$ | 3.5e+4 $MPa$ | $E$ | 5.5e+4 $MPa$ | $E$ | 3.5e+4 $MPa$ |
| $\nu$ | 0.3 | $\nu$ | 0.3 | $\nu$ | 0.3 |
| $\bar{\sigma}_0$ | 5.25 $MPa$ | $\bar{\sigma}_0$ | 41.25 $MPa$ | $\bar{\sigma}_0$ | 3.5 $MPa$ |
| $\bar{\sigma}_\infty$ | 0.0 | $\bar{\sigma}_\infty$ | 0.0 | $\bar{\sigma}_\infty$ | 0.0 |
| $\beta$ | 0.67e+3 | $\beta$ | 1.0e+3 | $\beta$ | 1.0e+3 |
| $\rho$ | 2.0e-9 $Ns^2/mm^4$ | $\rho$ | 2.0e-9 $Ns^2/mm^4$ | $\rho$ | 2.0e-9 $Ns^2/mm^4$ |
| N | 1.0 | N | 1.0 | N | 1.0 |
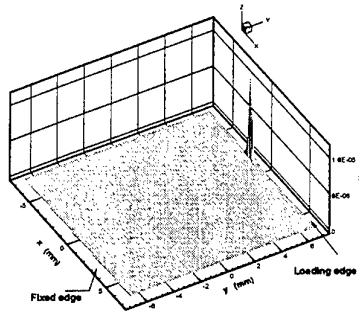


(a) V = 500 mm/s, $\eta = 200\ s^{-1}$, t = 2.0 $\mu$s



(b) V = 500 mm/s, $\eta = 200\ s^{-1}$, t = 5.5 $\mu$s



(c) V = 500 mm/s, $\eta = 200\ s^{-1}$, t = 8.0 $\mu$s
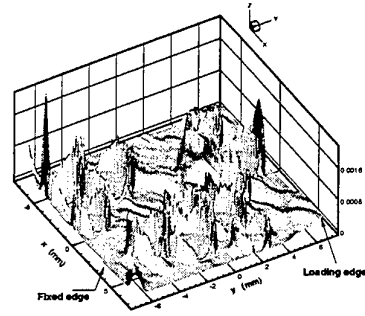


(d) V = 600 mm/s, $\eta = 200\ s^{-1}$, t = 8.0 $\mu$s

Figure 5.7: Development of plastic strain measure $\kappa$ for Perzyna viscoplastic model.

Structure one is analyzed first. The development of the plastic strain measure $\kappa$ for V = 500 mm/s, $\eta = 200\ s^{-1}$ is shown in Figs. 5.7a to c. Similar to that of a standard plastic model, strain localizations occur in the ITZs before the loading waves arrive at the fixed edge. After reflection, two strain localization zones initiate from the fixed corners of the structure. At time t = 8.0 $\mu$s, the waves have reflected from the loading edge, it can be seen that a few lower strain level localization zones have initiated from the
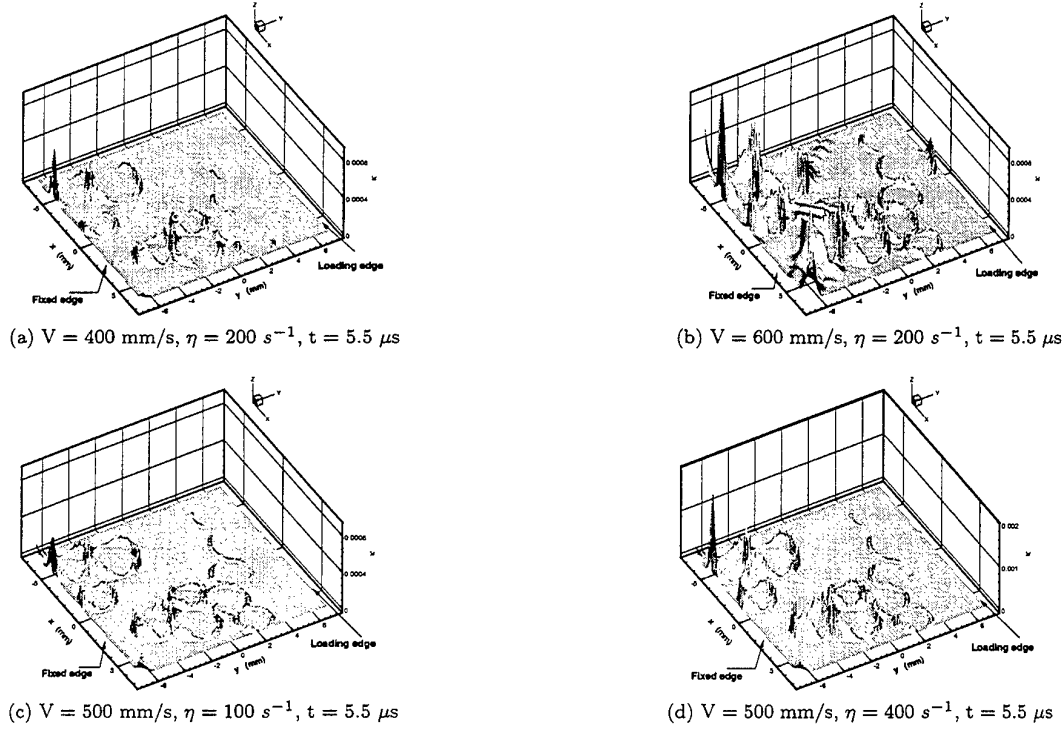
(a) V = 400 mm/s, $\eta = 200\ s^{-1}$, t = 5.5 $\mu$s

(b) V = 600 mm/s, $\eta = 200\ s^{-1}$, t = 5.5 $\mu$s

(c) V = 500 mm/s, $\eta = 100\ s^{-1}$, t = 5.5 $\mu$s

(d) V = 500 mm/s, $\eta = 400\ s^{-1}$, t = 5.5 $\mu$s

Figure 5.8: Influence of impact velocity and viscosity parameter on the development of plastic strain measure $\kappa$ for Perzyna viscoplastic model.



(a) Different impact velocities

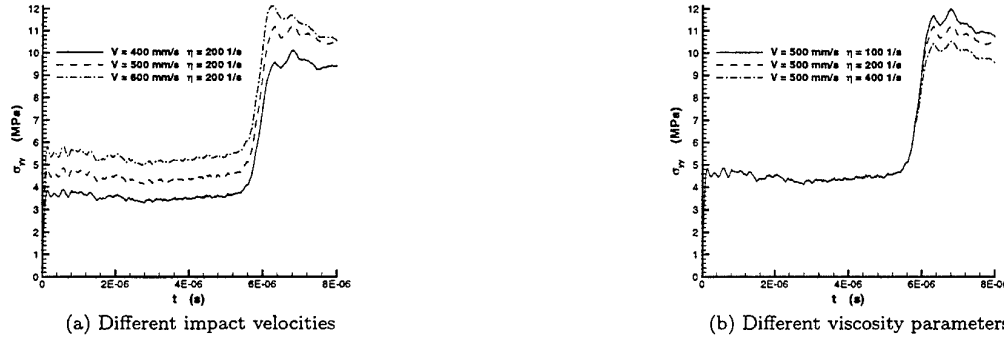(b) Different viscosity parameters

Figure 5.9: Influence of impact velocity and viscosity parameter on the reaction stress history along the loading edge for Perzyna viscoplastic model.

loading edge while the localization zones formed from the fixed corners were constraint around those corners. These localization zones in the matrix no longer propagate in one row of element and each zone is spread over a few elements in its transverse direction. The plastic straining is mainly concentrated in the ITZs, the localization zones which are formed in the ITZs are unlikely to propagate into the matrix. Increasing the impact velocity to V = 600 mm/s shows that there are a few more localization zones being formed in the matrix after the loading waves have reflected on the fixed edge and they can connect with each other, but the most intense plastic straining is still located in the ITZ (see Fig. 5.7d and Fig. 5.8b).

This result compares well with the analysis conducted by Weimin Wang (cf. [15]), which shows that the localization zone may be determined by the imperfection size or the internal length scale introduced by viscous effect depending on which one is smaller. In the two-dimensional case, the influence of the imperfection is very significant near the imperfection zone, while the internal length scale tends to be dominant at some distance away from the imperfection. Obviously, because of a lower strength, ITZs act
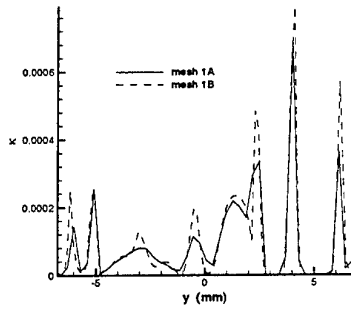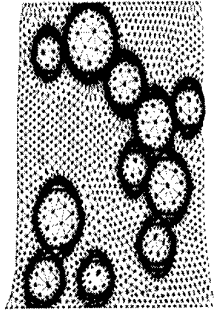
(a) Profiles of $\kappa$ along the central vertical cross section at time t = 8.0 $\mu$s
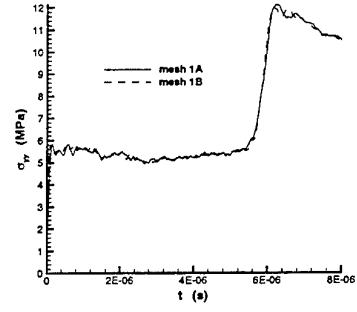
(b) History of average reaction stress component $\sigma_{yy}$ along the loading edge

Figure 5.10: Mesh objectivity for the Perzyna viscoplastic model with V = 600 mm/s, $\eta = 200\ s^{-1}$.



(a) Deformation pattern
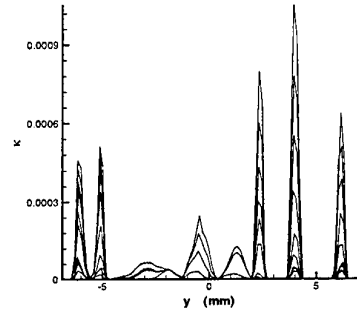
(b) Stroboscopic plot

Figure 5.11: The deformation pattern at time t = 8.0 $\mu$s for mesh 1A (a) and stroboscopic development of plastic strain measure $\kappa$ along the central vertical cross section for mesh 1B (b) with V = 600 mm/s and $\eta = 400\ s^{-1}$ .
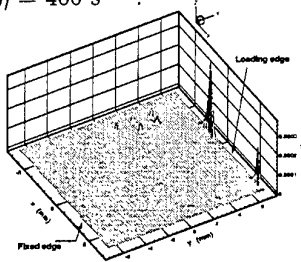


(a) t = 2.0 $\mu$s
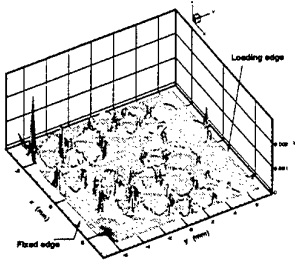
(b) t = 5.5 $\mu$s
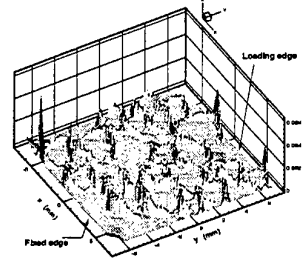
(c) t = 8.0 $\mu$s
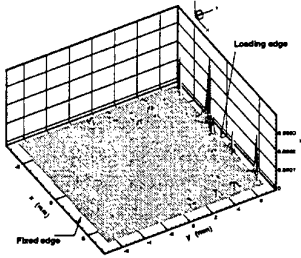
(d) t = 2.0 $\mu$s
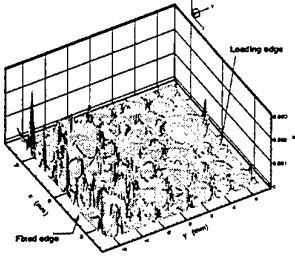
(e) t = 5.5 $\mu$s
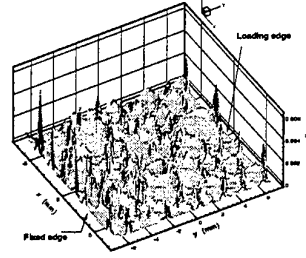
(f) t = 8.0 $\mu$s

Figure 5.12: Development of plastic strain measure $\kappa$ for structure two (a)-(c) and structure three (d)-(f) with V = 600 mm/s and $\eta = 400\ s^{-1}$.

(a) Structure two     (b) Structure three     (c) Reaction stress
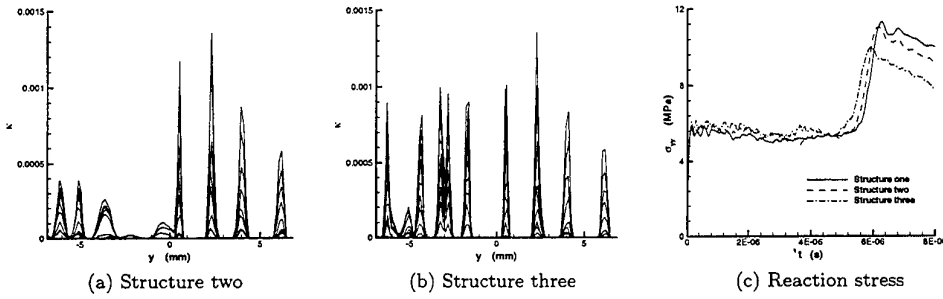
Figure 5.13: Stroboscopic development of plastic strain measure $\kappa$ along the central vertical cross section for structure two (a) and structure three (b); The reaction stress component $\sigma_{yy}$ along the loading edge for the three structures (c).



(a) Structure two     (b) Structure three

Figure 5.14: The deformation pattern at time t = 8.0 $\mu$s for structure two (a) and three (b) with V = 600 mm/s and $\eta = 400$ $s^{-1}$.

as imperfections in the microstructure of concrete. The aggregates in concrete have a high strength and elastic modulus. On one hand, the partial reflection of loading waves on them results in earlier and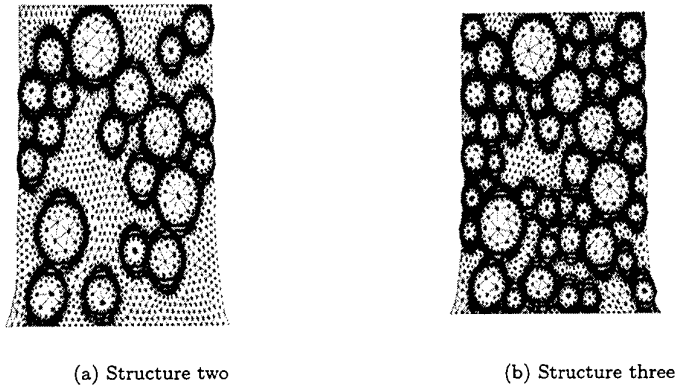 more intense plastic straining in the ITZ. On the other hand, they obstruct the propagation of a localization zone formed in the matrix. The fact that some localization zones in the matrix are concentrated around the corners of the fixed edge (see Fig. 5.7d) is an example of the latter role.

The influence of the impact velocity and the viscosity parameter is given in Fig. 5.8. The results show that the plastic straining is more intense when the impact velocity or viscosity parameter are increased. From the average reaction stress component $\sigma_{yy}$ along the loading edge versus time plots (see Fig. 5.9), we observe that the maximum reaction stress level increases apparently with the increase of the impact velocity and the decrease of the viscosity parameter (which corresponds to an increase of the viscous effect.)

Mesh objectivity of the numerical solution is checked in Fig. 5.10 with V = 600 mm/s and $\eta = 200$ $s^{-1}$. It shows that a finer mesh is needed in the ITZs in order to capture the high strain gradient.

The deformation pattern amplified with a factor of 1200 is presented for V = 600 mm/s and $\eta = 400$ $s^{-1}$ at time t = 8.0 $\mu$s in Fig. 5.11a, where the discretization mesh 1A is used. Large deformation mainly occurs in the ITZs of the microstructure. The width of the ITZ is very small, so that the higher strain level in these regions does not result in significant displacement change. Fig. 5.11b presents the stroboscopic plot of development of the plastic strain measure $\kappa$ along the central vertical cross section of the microstructure for the same impact velocity and viscosity parameter. As in all stroboscopic plots presented in this chapter, the interval between the first three profiles is 1.0 $\mu$s and 0.5 $\mu$s between other profiles. Comparing with Fig. 5.1b, it can be seen that strain localization in the matrix occurs mainly after the loading waves have propagated back from the fixed edge and have reflected on the loading edge. It is noted that the strain level in the microstructure is not very high.
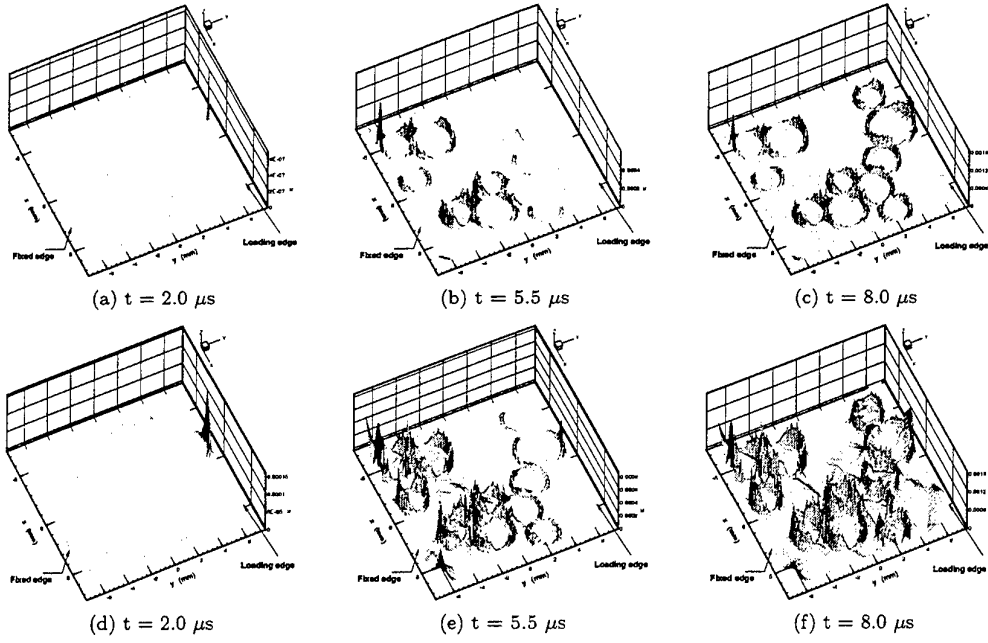
Figure 5.15: Development of plastic strain measure $\kappa$ in microstructure one with mesh 1A for V = 400 mm/s (a)-(c), V = 600 mm/s (d)-(f) and $\eta = 200$ $s^{-1}$.
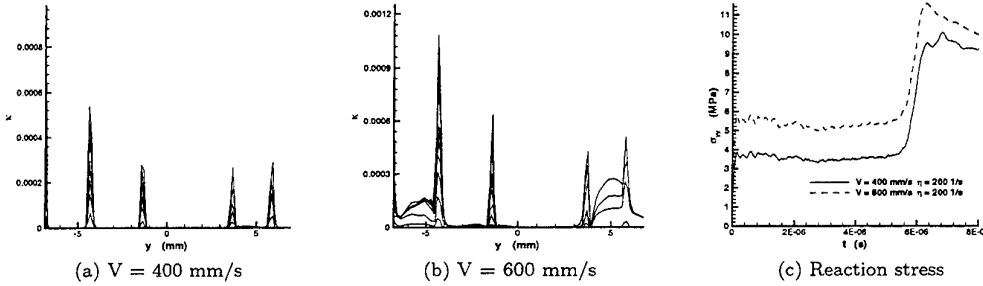


Figure 5.16: Stroboscopic development of plastic strain measure $\kappa$ along the vertical line across the center of the aggregate at the lower left corner of microstructure one with $\eta = 200$ $s^{-1}$; The reaction stress component $\sigma_{yy}$ along the loading edge for the two computations.

For the microstructures two and three the impact tensile velocity V = 600 mm/s and the viscosity parameter $\eta = 400$ $s^{-1}$ are utilized. The development of plastic strain measure $\kappa$ is shown in Fig. 5.12. As in structure one the strain localization is concentrated in the ITZs. The localization zones initiated from the fixed corners of the structure are confined by the aggregates and can not develop into a dominant shear band. In microstructure three a few more aggregates are placed around one of the two fixed corners, it can be seen that the localization zone can not initiate in the matrix around that corner. The stroboscopic development of $\kappa$ along the central vertical cross section for these examples are presented in Figs. 5.13a and b. The deformation patterns are given in Fig. 5.14.

The plot in Fig. 5.13c compares the average reaction stress component $\sigma_{yy}$ along the loading edge for the three structures with mesh 1A for structure one. We can observe that the peak stress level decreases with the increase of the volume of aggregates. This is because that plastic straining is mainly concentrated in the ITZs and all aggregates are surrounded by an ITZ, so that the negative effect of the volume fraction of ITZ on the average reaction stress level is more significant than the positive effect of the volume fraction of aggregates. However, it should be noted that an impact tensile velocity V = 600 mm/s and a viscosity parameter $\eta = 400$ $s^{-1}$ are used for the three computations. From the former results in this section for the influence of impact velocity and viscosity parameter, it can be expected that when the impact velocity and viscosity parameter are decreased, because of a less intense plastic

straining in the ITZs, the peak value of the average reaction stress along the loading edge may increase with the increase of the volume fraction of aggregates.

In an attempt to simulate the fracture of the aggregates in the microstructure under impact tensile loading, another two computations are conducted. Microstructure one with mesh 1A is used and the strength of the aggregates is reduced to the same as the matrix material, i.e. 5.25 MPa. The development of plastic strain meature $\kappa$ is shown in Fig. 5.15 for the impact velocity V = 400 mm/s, 600 mm/s and the viscosity parameter $\eta = 200\ s^{-1}$. The stroboscopic plots of $\kappa$ along the vertical line across the center of the aggregate at the lower left corner (see Fig. 5.1a) are given in Fig. 5.16. These results show that although the plastic straining is still mainly concentrated in the ITZs, a shear band initiated from one of the fixed corner does propagate through the aggregates and across the whole microstructure at an impact velocity V = 600 mm/s. When the impact velocity is reduced to V = 400 mm/s, this phenomenon does not occur. The reaction stress history for the two computations is shown in Fig. 5.16c. Comparing with the results in Fig. 5.9a, it can be seen that the peak value of the average reaction stress does not change significantly with the decrease of the matrix strength.

## 5.3  Duvaut-Lions viscoplastic model

The Duvaut-Lions viscoplastic model combined with a Rankine yield criterion, an associative flow rule, an exponential softening law and a strain hardening/softening hypothesis is used in this section. The material parameters are shown in Table 5.3 and different impact velocities V and relaxation times $\tau$

Table 5.3: Material parameters for Duvaut-Lions viscoplastic model

| Matrix | | Aggregate | | ITZ | |
|---|---|---|---|---|---|
| $E$ | 3.5e+4 $MPa$ | $E$ | 5.5e+4 $MPa$ | $E$ | 3.5e+4 $MPa$ |
| $\nu$ | 0.3 | $\nu$ | 0.3 | $\nu$ | 0.3 |
| $\bar{\sigma}_0$ | 5.25 $MPa$ | $\bar{\sigma}_0$ | 41.25 $MPa$ | $\bar{\sigma}_0$ | 3.5 $MPa$ |
| $\bar{\sigma}_\infty$ | 0.0 | $\bar{\sigma}_\infty$ | 0.0 | $\bar{\sigma}_\infty$ | 0.0 |
| $\beta$ | 0.67e+3 | $\beta$ | 1.0e+3 | $\beta$ | 1.0e+3 |
| $\rho$ | 2.0e-9 $Ns^2/mm^4$ | $\rho$ | 2.0e-9 $Ns^2/mm^4$ | $\rho$ | 2.0e-9 $Ns^2/mm^4$ |



(a) V = 600 mm/s, $\tau$ = 0.5 $\mu$s, t = 5.5 $\mu$s

(b) V = 600 mm/s, $\tau$ = 0.5 $\mu$s, t = 8.0 $\mu$s

(c) V = 500 mm/s, $\tau$ = 0.5 $\mu$s, t = 8.0 $\mu$s

(d) V = 600 mm/s, $\tau$ = 1.0 $\mu$s, t = 8.0 $\mu$s

Figure 5.17: Development of plastic strain measure $\kappa$ for Duvaut-Lions viscoplastic model.

34



(a) $\tau = 0.5\ \mu s$     (b) $\tau = 1.0\ \mu s$     (c) Different relaxation times
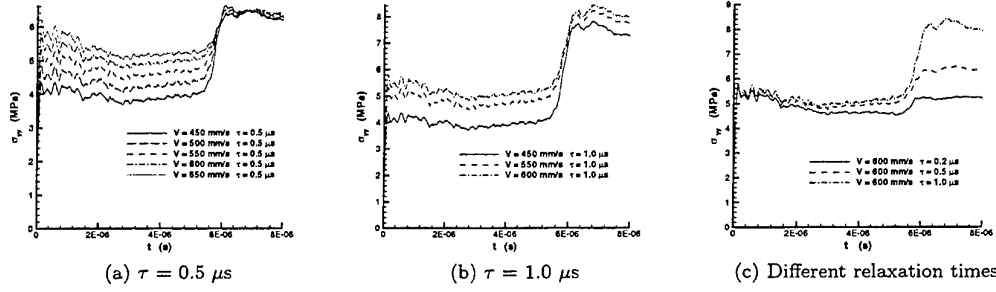
Figure 5.18: Influence of the impact velocity (a) and (b), and the relaxation time (c) on the reaction stress history along the loading edge for Duvaut-Lions viscoplastic model.
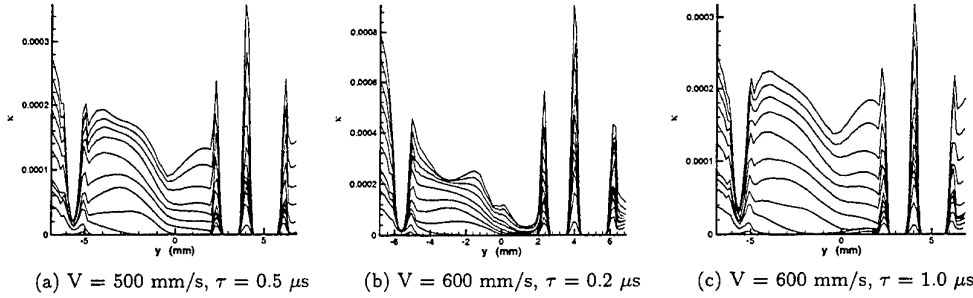


(a) $V = 500$ mm/s, $\tau = 0.5\ \mu s$     (b) $V = 600$ mm/s, $\tau = 0.2\ \mu s$     (c) $V = 600$ mm/s, $\tau = 1.0\ \mu s$

Figure 5.19: Stroboscopic development of plastic strain measure $\kappa$ along the central vertical cross section with different impact velocities and relaxation times.



(a) Profiles of $\kappa$ along the central vertical cross section at time t = 8.0 $\mu s$

(b) History of average reaction stress component $\sigma_{yy}$ along the loading edge
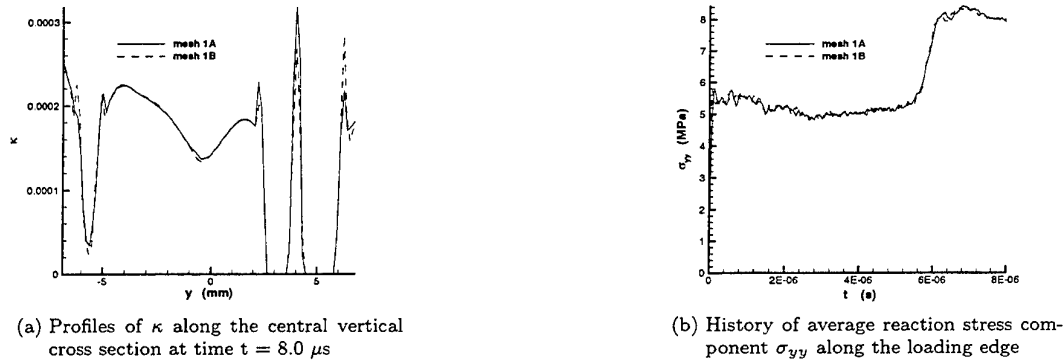
Figure 5.20: Mesh objectivity for Duvaut-Lions viscoplastic model with $V = 600$ mm/s and $\tau = 1.0\ \mu s$.

are used in the simulations. The microstructure one is analyzed first. The development of viscoplastic strain measure $\kappa$ with $V = 600$ mm/s and $\tau = 0.5\ \mu s$ is shown in Fig. 5.17a and b. Comparing with the localization patterns for the Perzyna model (cf. Fig. 5.7) it can be seen that the highest plastic strain level still occurs in the ITZs but a really diffuse mode of failure occurs in the matrix and there are no shear bands formed in the matrix. The plastic strain level in the matrix is comparable to that in the ITZs. The matrix material failed after the reflection of the loading waves on the fixed edge, the plastic strain increases consistently in the course of time. These characteristics are due to the choice of a Rankine yield criterion where the maximum principal tensile stress dominates the solution after yielding.

When the impact velocity is increased or the relaxation time is decreased the plastic strain level is higher (see Fig. 5.17), whereas the plastic strain along the fixed edge increases most significantly. When relaxation time $\tau$ is reduced to 0.2 $\mu s$, the localization zone along the fixed edge becomes the dominant one in the matrix with the amplitude the same as that in the ITZs. This can be observed in the stroboscopic plot for plastic strain measure $\kappa$ in Fig. 5.19b. This mode-I failure of the microstructure is due to the use of the Rankine yield criterion and the absence of the aggregates along the fixed edge.
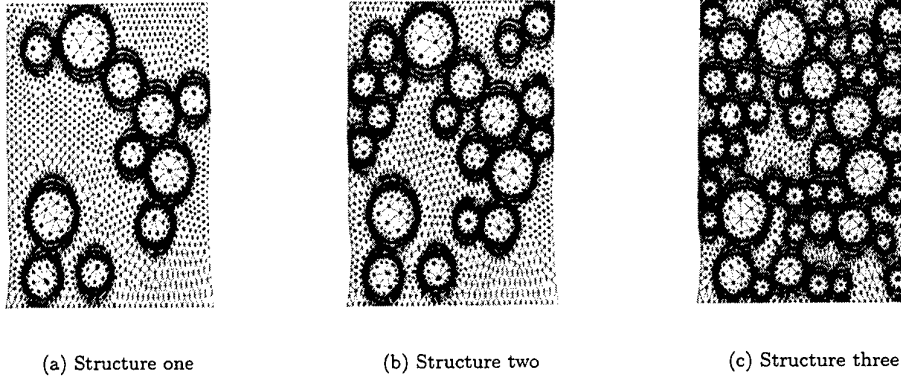
(a) Structure one        (b) Structure two        (c) Structure three

Figure 5.21: The deformation pattern at time t = 8.0 $\mu$s for mesh 1A (a), structure two (b) and structure three (c) with V = 600 mm/s and $\tau$ = 0.2 $\mu$s.



(a) t = 2.0 $\mu$s        (b) t = 5.5 $\mu$s        (c) t = 8.0 $\mu$s

(d) t = 2.0 $\mu$s        (e) t = 5.5 $\mu$s        (f) t = 8.0 $\mu$s
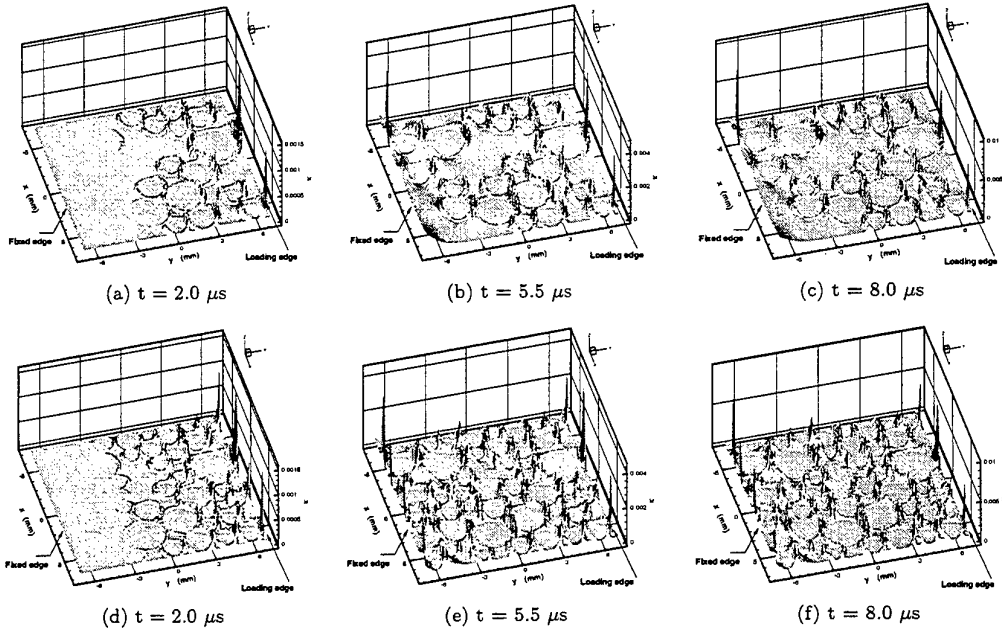
Figure 5.22: Development of plastic strain measure $\kappa$ for structure two (a)-(c) and structure three (d)-(f) with V = 600 mm/s and $\tau$ = 0.2 $\mu$s.

The influence of impact velocity and relaxation time on the reaction force along the loading edge is presented in Fig. 5.18. It is observed that the peak value of average reaction stress component $\sigma_{yy}$ is not affected by the impact velocity when a relaxation time $\tau$ = 0.5 $\mu$s is used, the reason is that the decrease of the backbone stress level due to softening material law neutralizes the increase of stress due to the increase of loading rate. When the relaxation time is increased to $\tau$ = 1.0 $\mu$s, the peak value of the average reaction stress increases with the increase of impact velocity. Combining the results in sections 5.1 and 5.2, it can be concluded that the viscous effect plays a dominant role in simulation of the positive loading rate effect of the concrete microstructure. The viscous effect can be seen for different values of the relaxation time in Fig. 5.18c, where the peak stress level increases significantly when the relaxation time is doubled.

The stroboscopic plots of the development of plastic strain measure $\kappa$ along the central vertical cross section for three numerical examples are given in Fig. 5.19. The characteristics of the development of

(a) Structure two        (b) Structure three        (c) Reaction stress

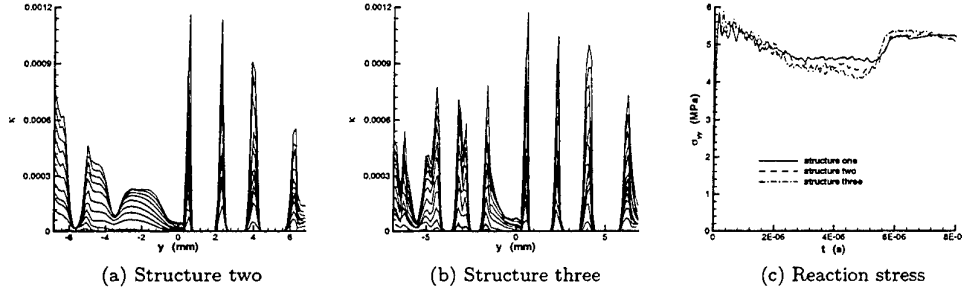Figure 5.23: Stroboscopic development of plastic strain measure $\kappa$ along the central vertical cross section for structure two (a) and structure three (b); The average reaction stress component $\sigma_{yy}$ along the loading edge for the three structures.
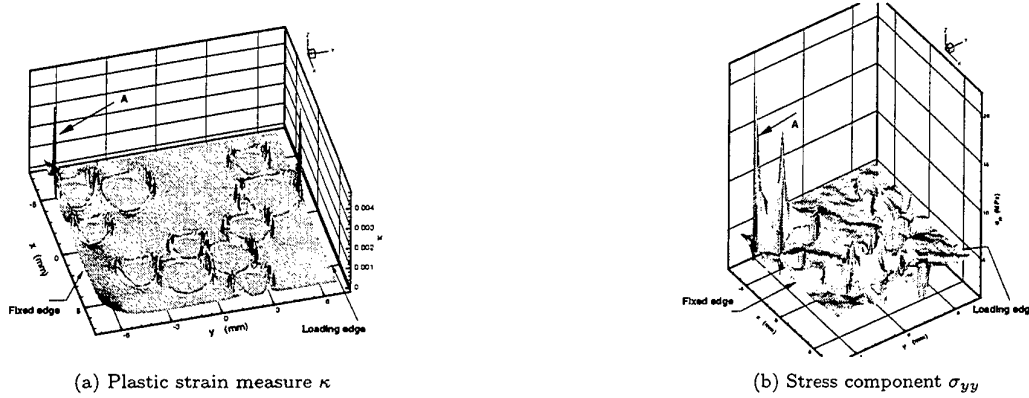


(a) Plastic strain measure $\kappa$                (b) Stress component $\sigma_{yy}$

Figure 5.24: Spurious hardening effect with large plastic strain for V = 600 mm/s and $\tau$ = 0.2 $\mu$s at time t = 5.5 $\mu$s.

plastic strain are exhibited.

The mesh objectivity is shown in Fig. 5.20 with the plots for the profiles of plastic strain measure $\kappa$ along the central vertical cross section and the average reaction stress component $\sigma_{yy}$ along the loading edge versus time. A finer mesh is needed in the interface transition zones.

The deformation of the microstructure amplified with a factor of 1200 for V = 600 mm/s, $\tau$ = 0.2 $\mu$s and at time 8.0 $\mu$s is shown in Fig. 5.21a. The deformation is localized in the ITZs and the matrix near the fixed edge.

For the microstructures two and three the impact tensile velocity V = 600 mm/s and the relaxation time $\tau$ = 0.2 $\mu$s are utilized. The development of plastic strain measure $\kappa$ is shown in Fig. 5.22. Because of the mode-I localization pattern along the fixed edge, the additional aggregates in microstructure two have no significant influence on this pattern and the plastic strain level. There are more ITZs along the fixed and loading edges for structure three, the plastic strain in these ITZs have high values. However, the plastic strain level in the matrix near the fixed edge decreases.

The stroboscopic development of $\kappa$ along the central vertical cross section for these examples is presented in Figs. 5.23a and b. The plot in Fig. 5.23c compares the average reaction stress component $\sigma_{yy}$ along the loading edge for the three structures with mesh 1A for structure one. We can observe that the average stress level is nearly the same in the beginning. Then it decreases gradually. This is due to the reflection of loading waves on the ITZs with an intense plastic straining in these three computations. As the fraction of the ITZ increases (i.e. from structure one to structure three), the average reaction stress level decreases during this process. However, when the reflected waves on the fixed edge reach the loading edge, the average reaction stresses for the three structures increase to nearly the same level. It indicates that the negative effect of the volume fraction of ITZ on the peak value of reaction stress neutralizes the positive effect of the volume fraction of aggregates. As for the Perzyna model in section 5.2, it is expected
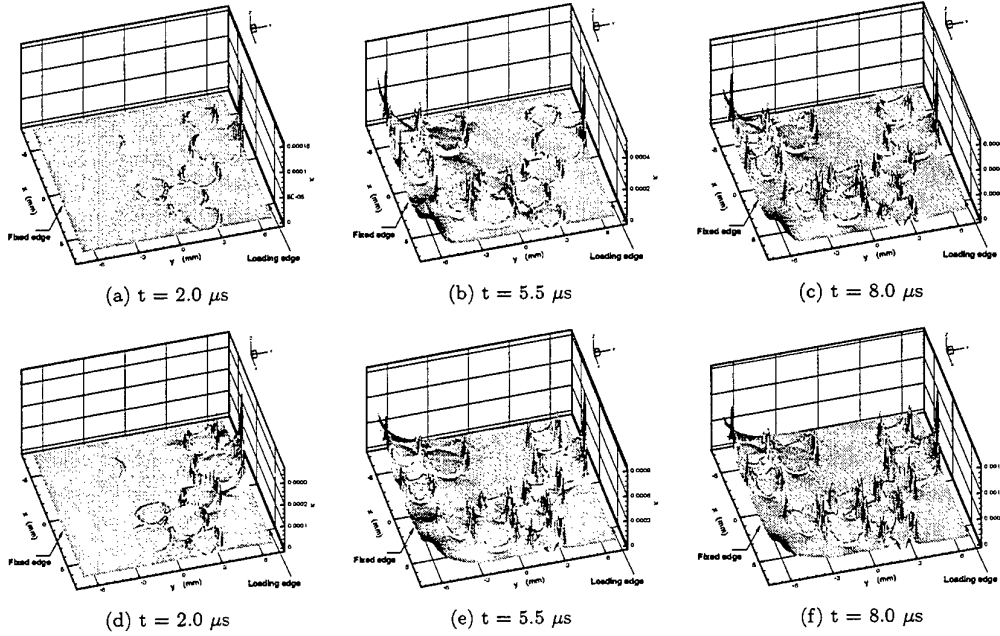
(a) t = 2.0 μs      (b) t = 5.5 μs      (c) t = 8.0 μs

(d) t = 2.0 μs      (e) t = 5.5 μs      (f) t = 8.0 μs

Figure 5.25: Development of plastic strain measure $\kappa$ in microstructure one with mesh 1A for V = 400 mm/s (a)-(c), V = 600 mm/s (d)-(f) and $\tau$ = 0.5 μs.



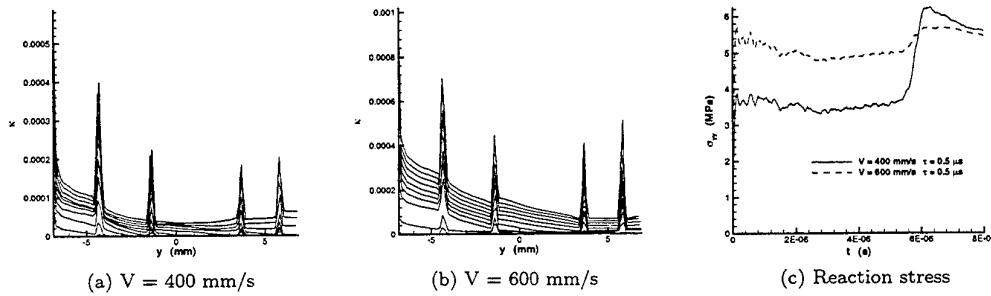(a) V = 400 mm/s      (b) V = 600 mm/s      (c) Reaction stress

Figure 5.26: Stroboscopic development of plastic strain measure $\kappa$ along the vertical line across the center of the aggregate at the lower left corner of microstructure one with $\tau$ = 0.5 μs; The average reaction stress component $\sigma_{yy}$ along the loading edge for the two computations.

when the impact velocity is decreased or the relaxation time is increased the peak value of the average reaction stress along the loading edge will increase with the increase of the volume fraction of aggregates. The deformation patterns for these two structures at time t = 8.0 μs can be seen in Figs. 5.21b and c.

It should be mentioned that for simulations using the viscoplastic models, we can observe a physically unrealistic strain rate hardening effect when the plastic strain in some ITZs is very large. This phenomenon is especially significant for the ITZs located on the fixed or loading edge. The plots in Fig. 5.24 provide an example, where the arrow A points to the ITZ which achieves a high plastic strain and stress level at the same time.

Two computations are carried out to simulate the fracture behavior of aggregates. The microstructure one with mesh 1A is used and the strength of the aggregates is reduced to the same as the matrix material, i.e. 5.25 MPa. The impact velocities V = 400 mm/s, 600 mm/s and relaxation time $\tau$ = 0.5 μs are adopted. A varied smaller time step is used for the computation with V = 600 mm/s. The development of plastic strain measure $\kappa$ is shown in Fig. 5.25. The stroboscopic plots of $\kappa$ along the vertical line across the center of the aggregate at the lower left corner (see Fig. 5.1a) are given in Fig. 5.26. These results show that aggregate fracture occurs after the loading waves have reflected on the fixed edge. The plastic straining in the ITZs is more intense than that in the matrix and the aggregates. But in the latter two phases, the trends of plastic straining are very consistent. Compared with the computations using the Perzyna

model, the aggregate fracture still occurs when the impact velocity is reduced to 400 mm/s. Due to the aggregate fracture, the peak value of the average reaction stress decreases when the impact velocity is increased from 400 mm/s to 600 mm/s (cf. Fig. 5.18a).

## 5.4 Constant gradient damage model

The second-order implicit constant gradient damage model described in section 3.2.1 is used in this section. A linear interpolation for the nonlocal equivalent strain is adopted in addition to the linear interpolation for the displacement field. The natural boundary condition (Eq. 3.48) is enforced on four edges of the microstructure by using a penalty factor technique. An additional term

$$\alpha \int_{\partial\Omega} \delta(\mathbf{n}^T\nabla\bar{\epsilon}_{eq})(\mathbf{n}^T\nabla\bar{\epsilon}_{eq})d\Gamma \tag{5.1}$$

where $\alpha$ is the penalty factor, is augmented to the weak form of the diffusion equation (Eq. 3.59). The exponential softening damage evolution law and the modified Von Mises definition of equivalent strain are utilized. The material parameters are shown in Table 5.4.

Table 5.4: Material parameters for implicit constant gradient damage model

| Matrix | | Aggregate | | ITZ | |
|---|---|---|---|---|---|
| $E$ | 3.5e+4 $MPa$ | $E$ | 5.5e+4 $MPa$ | $E$ | 3.5e+4 $MPa$ |
| $\nu$ | 0.3 | $\nu$ | 0.3 | $\nu$ | 0.3 |
| $\kappa_i$ | 1.5e-4 | $\kappa_i$ | 7.5e-4 | $\kappa_i$ | 1.0e-4 |
| $\alpha$ | 0.96 | $\alpha$ | 0.96 | $\alpha$ | 0.96 |
| $\beta$ | 500.0 | $\beta$ | 500.0 | $\beta$ | 500.0 |
| $\rho$ | 2.0e-9 $Ns^2/mm^4$ | $\rho$ | 2.0e-9 $Ns^2/mm^4$ | $\rho$ | 2.0e-9 $Ns^2/mm^4$ |
| $k$ | 1.0 | $k$ | 1.0 | $k$ | 1.0 |



(a) $\epsilon_{eq}$, t = 2.0 $\mu$s     (b) $\epsilon_{eq}$, t = 5.5 $\mu$s     (c) $\epsilon_{eq}$, t = 8.0 $\mu$s

(d) $\omega$, t = 2.0 $\mu$s     (e) $\omega$, t = 5.5 $\mu$s     (f) $\omega$, t = 8.0 $\mu$s

Figure 5.27: Development of equivalent strain (a)-(c) and damage (d)-(f) with V = 400 mm/s and c = 0.05 mm$^2$ for constant gradient damage model and mesh 1A.

The development of equivalent strain $\epsilon_{eq}$ and damage $\omega$ with impact velocity V = 400 mm/s and gradient parameter c = 0.05 mm$^2$ for structure one mesh 1A is presented in Fig. 5.27. We observe that

(a) $\epsilon_{eq}$, t = 2.0 $\mu$s    (b) $\epsilon_{eq}$, t = 5.5 $\mu$s    (c) $\epsilon_{eq}$, t = 8.0 $\mu$s

(d) $\omega$, t = 2.0 $\mu$s    (e) $\omega$, t = 5.5 $\mu$s    (f) $\omega$, t = 8.0 $\mu$s

Figure 5.28: Development of equivalent strain (a)-(c) and damage (d)-(f) with V = 500 mm/s and c = 0.05 mm$^2$ for constant gradient damage model and mesh 1A.



(a) $\epsilon_{eq}$, t = 2.0 $\mu$s    (b) $\epsilon_{eq}$, t = 5.5 $\mu$s    (c) $\epsilon_{eq}$, t = 8.0 $\mu$s

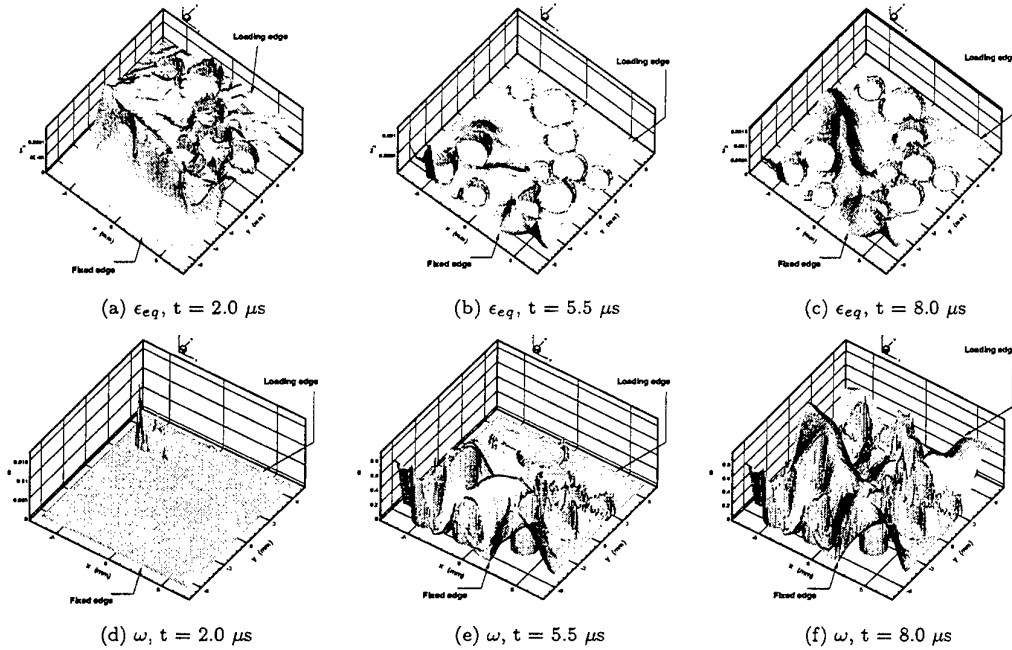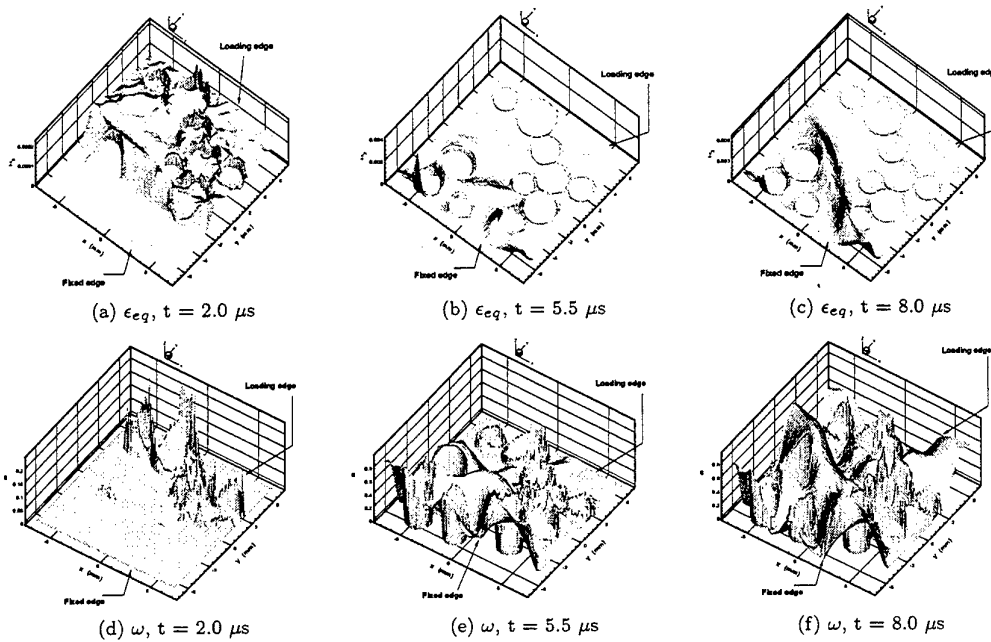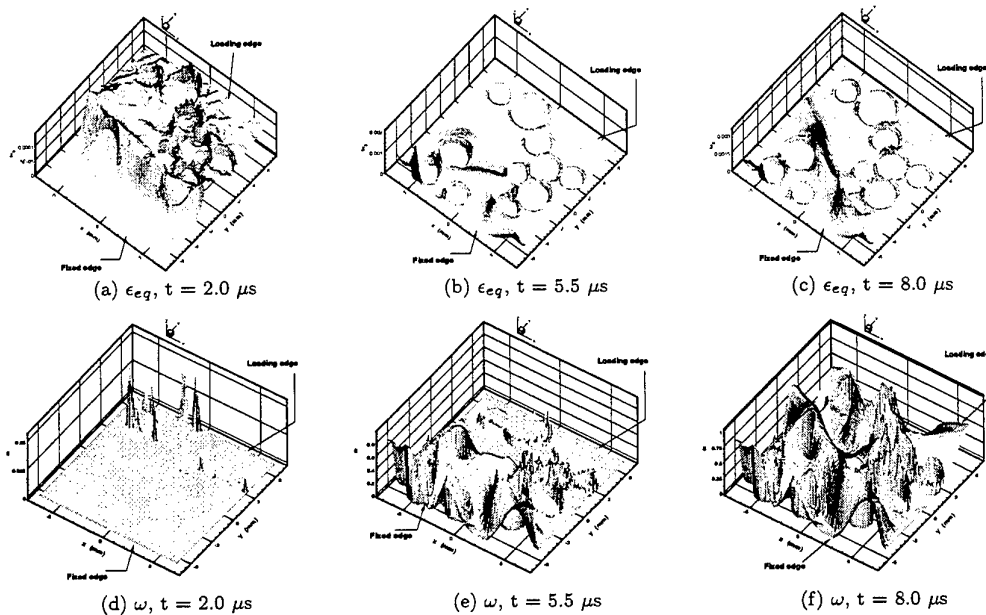(d) $\omega$, t = 2.0 $\mu$s    (e) $\omega$, t = 5.5 $\mu$s    (f) $\omega$, t = 8.0 $\mu$s

Figure 5.29: Development of equivalent strain (a)-(c) and damage (d)-(f) with V = 400 mm/s and c = 0.02 mm$^2$ for constant gradient damage model and mesh 1A.

before the loading waves reach the fixed edge strain localization and damage have occured in some ITZs. After the reflection on the fixed edge, another localization zone is initiated in the matrix from one of the fixed corners of the microstructure. It propagates in the matrix, connects with other localization zones including the ones that are developed in the ITZs and finaly at time t = 8.0 $\mu$s grows into a dominant shear band across the microstructure. At that time the loading waves have reflected on the fixed edge and loading edge, and approach the fixed edge again. This result is also consistent with the analysis carried out by Weimin Wang (cf. [15]), which shows that the width of the localization zone for gradient
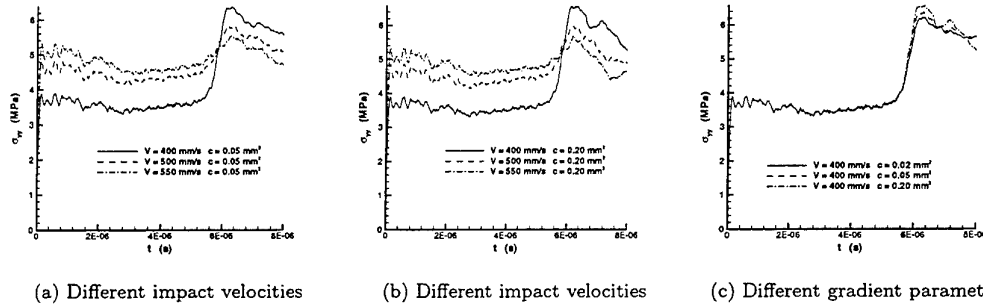
(a) Different impact velocities  (b) Different impact velocities  (c) Different gradient parameters

Figure 5.30: Influence of impact velocity and gradient paramter on the reaction stress history along the loading edge for constant gradient damage model with mesh 1A.
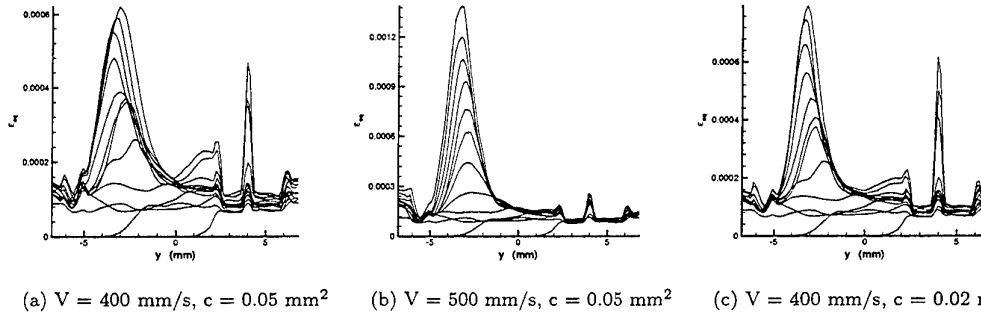


(a) $V = 400$ mm/s, $c = 0.05$ mm$^2$    (b) $V = 500$ mm/s, $c = 0.05$ mm$^2$    (c) $V = 400$ mm/s, $c = 0.02$ mm$^2$

Figure 5.31: Stroboscopic development of equivalent strain $\epsilon_{eq}$ along the central vertical cross section of the structure one mesh 1A.



(a) Profile of $\epsilon_{eq}$ along the central vertical cross section at time t = 8.0 $\mu$s

(b) Average reaction stress component $\sigma_{yy}$ history along the loading edge
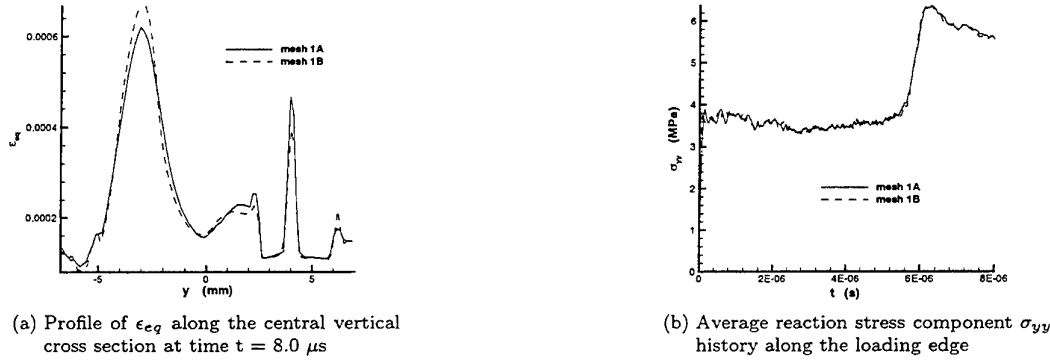
Figure 5.32: Mesh objectivity of constant gradient damage model for structure one with $V = 400$ mm/s and $c = 0.05$ mm$^2$.

enhanced models is irrespective of the size of imperfection. Note that the mode-II failure pattern is due to the fact that when $k = 1$, the definition of equivalent strain is a standard Von Mises model.

The impact velocity increases to $V = 500$ mm/s in a simulation presented in Fig. 5.28 with the same material parameters as that in Fig. 5.27. Before the reflection on the fixed edge, the loading waves cause much more damage in the ITZs. After reflection a similar failure process as that in Fig. 5.27 is observed, while the strain level and damage level are much higher.

When the impact velocity is still taken as $V = 400$ mm/s but the gradient parameter is reduced to 0.02mm$^2$, there are more damage and deformation occurring in the microstructure as that for an increased impact velocity. The evolution of equivalent strain and damage is given in Fig. 5.29. The failure pattern remains unchanged but the width of localization zones becomes narrower.
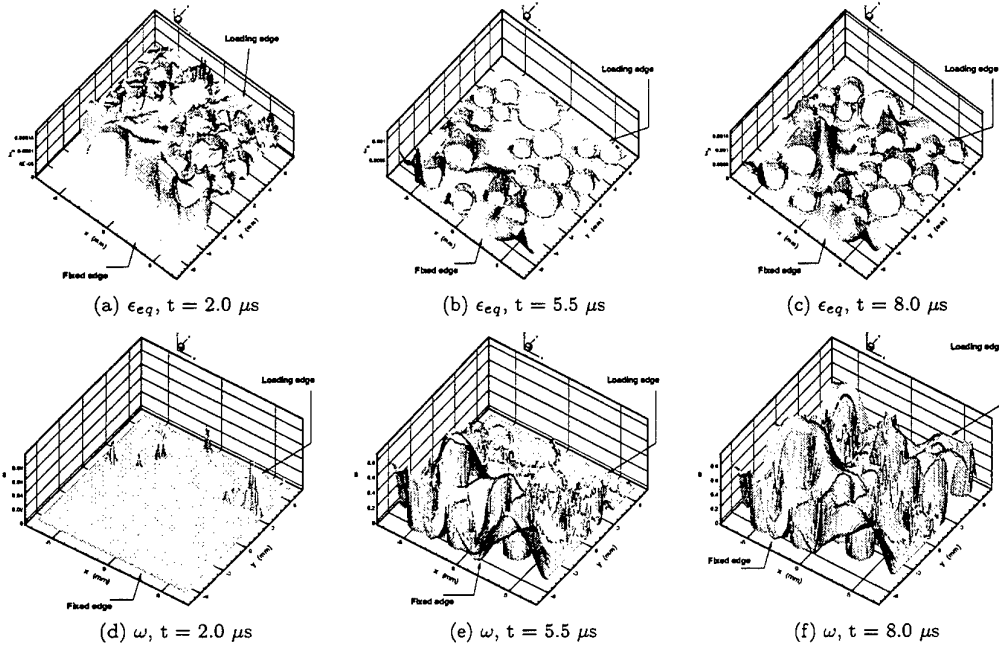
(a) $\epsilon_{eq}$, t = 2.0 $\mu$s   (b) $\epsilon_{eq}$, t = 5.5 $\mu$s   (c) $\epsilon_{eq}$, t = 8.0 $\mu$s

(d) $\omega$, t = 2.0 $\mu$s   (e) $\omega$, t = 5.5 $\mu$s   (f) $\omega$, t = 8.0 $\mu$s

Figure 5.33: Development of equivalent strain (a)-(c) and damage (d)-(f) with V = 400 mm/s and c = 0.05 mm$^2$ for constant gradient damage model and structure two.



(a) $\epsilon_{eq}$, t = 2.0 $\mu$s   (b) $\epsilon_{eq}$, t = 5.5 $\mu$s   (c) $\epsilon_{eq}$, t = 8.0 $\mu$s

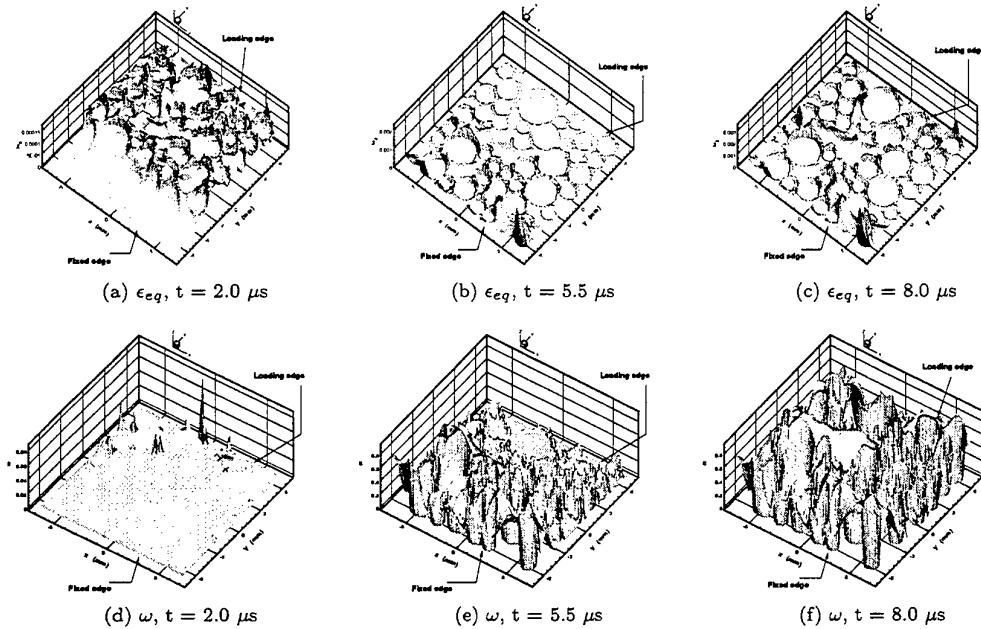(d) $\omega$, t = 2.0 $\mu$s   (e) $\omega$, t = 5.5 $\mu$s   (f) $\omega$, t = 8.0 $\mu$s

Figure 5.34: Development of equivalent strain (a)-(c) and damage (d)-(f) with V = 400 mm/s and c = 0.05 mm$^2$ for constant gradient damage model and structure three.

The influence of the impact velocity and the gradient parameter on the reaction stress history along the loading edge is presented in Fig. 5.30. Because of the damage in the microstructure, the waves reflected from the fixed edge arrive at the loading edge with a decreasing peak value for an increase of impact velocity or a decrease of gradient parameter. When the gradient parameter is increased from c = 0.05 mm$^2$ to c = 0.20 mm$^2$, the decreasing trend of the peak value of the average reation stress is not changed. This is because that the gradient parameter is associated with the nonlocal equivalent strain, while the viscosity parameter in the Perzyna model and the Duvaut-Lions model are connected with the
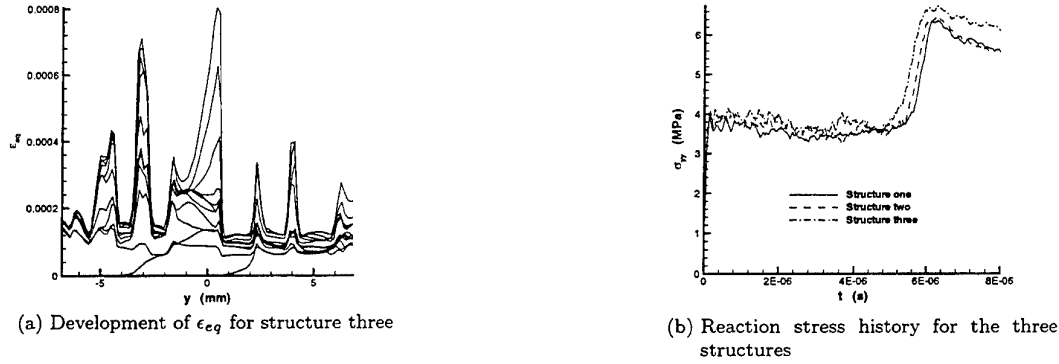
(a) Development of $\epsilon_{eq}$ for structure three



(b) Reaction stress history for the three structures

Figure 5.35: The stroboscopic development of equivalent strain $\epsilon_{eq}$ along the central vertical cross section of the structure three (a) and the average reaction stress component $\sigma_{yy}$ along the loading edge versus time for the three structures (b).
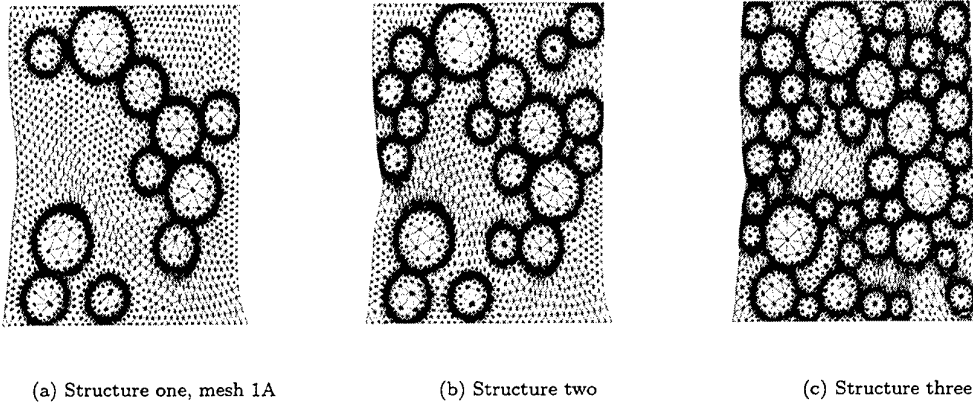


(a) Structure one, mesh 1A



(b) Structure two



(c) Structure three

Figure 5.36: Deformation patterns for the three structures with $V = 400$ mm/s, c $= 0.05$ mm$^2$ and at time t $= 8.0$ $\mu$s.

viscoplastic strain rate. It can be concluded that at relatively high impact tensile velocity, a positive loading rate dependence can hardly be obtained with this gradient dependent model.

The development of equivalent strain along the central vertical cross section of microstructure one with mesh 1A is presented by using stroboscopic plots in Fig. 5.31. The above analyzed characteristics of the numerical results can also be observed in this figure.

The mesh objectivity of the numerical solution with the use of a constant gradient damage model is checked by comparing the results obtained for the two meshes of structure one. The distribution of equivalent strain along the central vertical cross section of the microstructure at time t $= 8.0$ $\mu$s and the average reaction stress component $\sigma_{yy}$ along the loading edge versus time are ploted in Fig. 5.32. It shows that the solution is independent of the finite element discretization.

A similar numerical simulation is carried out on microstructure two and microstructure three with impact velocity $V = 400$ mm/s and gradient parameter c $= 0.05$ mm$^2$. The evolution of equivalent strain $\epsilon_{eq}$ and damage $\omega$ for structure two is shown in Fig. 5.33. It shows that the additional aggregates in the microstructure deviate the propagation of the dominant shear band. The strain level does not change significantly compared with Fig. 5.27, but there are more steep strain gradient variations in the microstructure due to the larger volume of ITZ. The aggregate volume is further increased in structure three, so is the volume of ITZ. The numerical results are shown in Fig. 5.34. Because of a very high strength, the aggregates do not fail during loading. They obstruct and deviate the propagation of localization zones. Hence, a diffuse mode of failure is formed for this structure. The stroboscopic development

of equivalent strain is given in Fig. 5.35a for structure three.

The comparison of the average reaction stress history along the loading edge for the three structures with the same material parameters and impact velocity is shown in Fig. 5.35b. The limit stress level increases with the volume of aggregates. Comparing with the results in sections 5.2 and 5.3, it can be concluded that the influence of a higher volume of aggregates is more significant when the damage pattern is more diffuse and this strengthening effect is greatly reduced when the damage is mainly concentrated in the ITZ, unless a viscous effect is incorporated in the model. The deformation patterns for the three structures at time t = 8.0 $\mu$s are shown in Fig. 5.36.

44

# Chapter 6

# Discussion

In this report different continuum constitutive models are used to investigate the dynamic response of concrete at meso-level under impact tensile loading.

For the one-dimensional bar problem, mesh dependence of the numerical results as one of the consequences of the ill-posedness of the initial value problem, is illustrated with a standard plastic model combined with a linear softening law and a local damage model. Incorporation of higher-order temporal derivatives or higher-order spatial derivatives into the continuum model can regularize the governing field equations and preserve the well-posedness of the initial value problem upon the onset of strain localization. The Perzyna viscoplastic model, the Duvaut-Lions viscoplastic model and the gradient enhanced damage model are used to exhibit the regularization effect. In addition to a constant gradient damage model, a strain-based transient-gradient damage model is also used to illustrate that making the gradient parameter a variable can avoid suprious spreading of damage at the final stage in a failure analysis.

Three block square microstructures are used to conduct two-dimensional analyses. Three phases are considered in the microstructure, namely matrix, aggregate and interfacial transition zone. Physically meaningful result can not be obtained by using a standard plastic model because the numerical results show an obvious mesh dependence. When a Perzyna model combined with a Von Mises yield criterion is used, two types of localization zones can be distinguished. One type includes those initiated from the ITZ and which are controlled by the width of the ITZ, while the other type consists of those formed in the matrix and are dominated by the internal length scale of the material. The plastic strain level in the ITZs is much higher than in the matrix. The localization zones formed in the matrix can propagate but can not develop into dominant shear bands due to the constraints imposed by the aggregates. The plastic deformation increases with the increase of impact velocity and decrease of a viscous effect. A finer discretization is needed in the ITZs in order to capture large strain gradients. The confining effect of aggregates on the localization zones in the matrix is further illustrated by the simulations on structure two and three. In the computations, a positive loading rate dependence is obtained which is due to the viscous effect incorporated in the constitutive relation. The peak value of average reaction stress along the loading edge decreases with the increase of volume fraction of the aggregates. However, it is expected that the enforcing effect of aggregates can be simulated when the viscous effect is increased in the material model. Additional simulations with a reduced strength for the aggregates show that the mode-II fracture of aggregates can be simulated with the Perzyna model.

When a Duvaut-Lions viscoplastic model combined with a Rankine yield criterion is used, a localization pattern which is different from that for the Perzyna model is obtained. The plastic strain level in the matrix is comparable with that in the ITZs, and it increases consistently with loading. Hence, a more diffuse failure mode can be formed. However when the impact velocity is increased or the relaxation time is reduced, a dominant localization zone of mode-I type emerges along the fixed edge. Wave reflections on the aggregates can cause earlier and more intense plastic straining in the matrix and the ITZs. At the same time, the increase of the aggregate volume can increase the average modulus and the load carrying capacity of the structure. These two effects can be observed in the numerical results. The peak value of average reaction stress exhibits no loading rate dependence with a specific choice of the relaxation time.

45

However, when the relaxation time is doubled a positive loading rate dependence is obtained. The same trend can be observed for the simulation of the enforcing effect of aggregates. When the strength of the aggregates is reduced, a mode-I fracture of aggregates can be observed in the numerical results.

The third model adopted is the second-order implicit constant gradient damage model. Utilizing the modified Von Mises definition of equivalent strain, a dominant shear band can be formed in microstructure one. The intensity of strain localization increases with the increase of impact velocity and the decrease of gradient parameter. The band width decreases when the gradient parameter is reduced. The additional aggregates in microstructure two change the propagation of the dominant shear band, whereas due to the high volume of aggregates in microstructure three the localization pattern is more diffuse. In the computations, the peak value of the average reaction stress decreases with the increase of the impact velocity. A positive loading rate dependence can hardly be obtained at relatively high impact velocity due to the absence of a viscous effect. When the volume fraction of aggregates is increased the maximum reaction stress level along the loading edge increases.

# Bibliography

[1] A. Simone. *Assessment of a Gradient-Enhanced Continuum Damage Model and Its Implementation.* Report CM 2000 009, Delft University of Technology, The Netherlands, 2000.

[2] H. Askes. *Advanced Spatial Discretisation Strategies for Localised Failure.* Ph.D. Dissertation, Delft University of Technology, The Netherlands, 2000.

[3] R. de Borst and L.J. Sluys. Computational Methods in Non-linear Solid Mechanics. Lecture notes, CT5142, Delft Universiy of Technology, The Netherlands, 2001.

[4] G. Duvaut and J.L. Lions. *Les inequations en Mechanique et en Physique.* Dunod, Paris, 1972.

[5] P.H. Feenstra. *Computational Aspects of Biaxial Stress in Plain and Reinforced Concrete.* Ph.D. Dissertation, Delft University of Technology, The Netherlands, 1993.

[6] M.D.G. Geers. *Experimental Analysis and Computational Modelling of Damage and Fracture.* Ph.D. Dissertation, Eindhoven University of Technology, The Netherlands, 1997.

[7] G. Meschke, R. Lackner and H.A. Mang. An anisotropic elastoplastic-damage model for plain concrete. *International Journal for Numerical Methods in Engineering,* 42:703-727, 1998.

[8] J. Pamin. *Gradient-dependent Plasticity in Numerical Simulation of localisation Phenomena.* Ph.D. Dissertation, Delft University of Technology, The Netherlands, 1994.

[9] R.H.J. Peerlings. *Enhanced Damage Modelling for Fracture and Fatigue.* Ph.D. Dissertation, Eindhoven University of Technology, The Netherlands, 1999.

[10] P. Perzyna. Foundamental problems in viscoplasticity. *Recent Advances in Applied Mechanics.* Academic Press, New York, 9:243-377, 1966.

[11] L.J. Sluys. *Wave Propagation, localisation and Dispersion in Softening Solids.* Ph.D. Dissertation, Delft University of Technology, The Netherlands, 1992.

[12] M.G.A. Tijssens. *On the Cohesive Surface Methodology for Fracture of Brittle Heterogeneous Solids.* Ph.D. Dissertation, Delft University of Technology, The Netherlands, 2001.

[13] O. Van der Sluis, P. Schreurs, W. Brekelmans and H. Meijer. Overall behavior of heterogeneous elastoviscoplastic materials: effect of micro-structural modelling. *Mechanics of material,* 32:449-462, 2000.

[14] M.R.A. Van Vliet. *Size Effect in Tensile Fracture of Concrete and Rock.* Ph.D. Dissertation, Delft Unversity of Technology, The Netherlands, 2000.

[15] W.M. Wang. *Stationary and Propagative Instabilities in Metals.* Ph.D. Dissertation, Delft Unversity of Technology, The Netherlands, 1997.

[16] G.N. Wells. *Discontinuous Modelling of Strain localisation and Failure.* Ph.D. Dissertation Delft University of Technology, The Netherlands, 2001.